Nano Research
2023, 16(3): 3741–3765

ISSN 1998-0124 CN 11-5974/O4
https://doi.org/10.1007/s12274-022-4526-9

Review Article

Realizing high-performance all-solid-state batteries with sulfide solid electrolyte and silicon anode: A review

Xinyang Wang[1,2], Kuang He[3], Siyuan Li[1,2], Jiahui Zhang[1,2], and Yingying Lu[1,2] (✉)

[1] State Key Laboratory of Chemical Engineering, Institute of Pharmaceutical Engineering, College of Chemical and Biological Engineering, Zhejiang University, Hangzhou 310027, China
[2] ZJU-Hangzhou Global Scientific and Technological Innovation Center, Hangzhou 311215, China
[3] Zhejiang Yongtai Technology Co., Ltd., Taizhou 317000, China

Received: 14 March 2022 / **Revised:** 6 May 2022 / **Accepted:** 11 May 2022

ABSTRACT

Sulfide solid electrolyte (SE) is one of the most promising technologies for all-solid-state batteries (ASSBs) because of its high ionic conductivity and ductile mechanical properties. In order to further improve the energy density of sulfide-based ASSBs and promote practical applications, silicon anodes with ultrahigh theoretical capacity (4,200 mAh·g^{-1}) and rich resource abundance have broad commercial prospects. However, significant challenges including bulk instability of sulfide SEs and poor utilization of silicon materials have severely impeded the ASSBs from becoming viable. In this review, we first introduce the critical bulk properties of sulfide SEs and the most recent improving strategies covering the ionic conductivity, air stability, electrochemical window, mechanical stability, thermostability and solvent stability. Next, we introduce the main factors affecting the compatibility of silicon and sulfide SE, including the carbon's effect, particle size of silicon, external pressure, silicon composite matrix and the depth of silicon's lithiation. Finally, we discuss possible research directions in the future. We hope that this review can provide a comprehensive picture of the role of nanoscale approaches in recent advances in ASSBs with sulfide and silicon, as well as a source of inspiration for future research.

KEYWORDS

all-solid-state battery, sulfide solid electrolyte, silicon anode, nanoscale optimization

1 Introduction

Replacing internal-combustion engines with electric power in vehicles is a growing trend and an essential method to achieve the carbon-neutral target [1, 2]. Nowadays, lithium-ion batteries (LIBs) as efficient energy storage systems have successfully revolutionized electric-powered transportation. However, the organic liquid electrolytes mainly used by the commercial packed LIBs are inflammable, volatile and easy to leak [3, 4]. In view of safety and durability, all-solid-state batteries (ASSBs) with the solid electrolytes (SEs) are believed of the prospect to break the bottleneck and push forward the post-electric era [5, 6].

The starting point for SEs can be dated back to the 1960s, when the β-alumina ($Na_2O·11Al_2O_3$) was applied in high-temperature Na-S batteries [7]. Over the past decades, plentiful efforts have been made to develop SEs with high ionic conductivity under acceptable temperature. The significant progress includes the inventions of solid-state oxide electrolytes, sulfide electrolytes, poly(ethylene oxide) (PEO)/alkali-metal ion electrolytes, borohydrides and their hybrids [8–13]. Among them, sulfide SEs attract much attention due to the exceptional room temperature ionic conductivity (1–10 mS·cm^{-1}) comparable even to those of organic liquid electrolytes. Moreover, the sulfide SE can be simply fabricated by cold pressing rather than high-temperature sintering process (e.g., over 1,000 °C for oxide SEs) to reduce the interfacial resistance between particles due to sulfide's ductile nature [14, 15]. Driven by the high safety, high energy density and easy-packaging advantages, Toyota, CATL, Solid Energy, etc. are committed to promoting the application of sulfide-based ASSBs in electric vehicles [14]. Despite of numerous research interests and progresses in both academia and industry, sulfide SEs' narrow electrochemical window, weak stability in air or polar solvent, unsatisfied mechanical properties and unstable interface with electrodes still impede their practical applications.

At the anode side, while many thoughts that the use of lithium metal anode would maximize the energy density of the sulfide-based ASSBs system, detrimental interfacial reactions and persistent dendritic short circuiting have made it a large gap between fundamental research and practical application [16, 17]. Except for lithium metal anode, silicon (Si) has also been vigorously recognized as one of the most promising next-generation anode materials due to its ultrahigh gravimetric capacity (4,200 mAh·g^{-1}), low working voltage (ca. 0.3 V vs. Li$^+$/Li) and abundant natural resources [18–21]. Nevertheless, the study on Si anode is mainly focused on liquid electrolyte systems while the research is relatively scarce in ASSBs. Li's group evaluated the energy density of ASSBs with sulfide SE and Si anode to more than 300 Wh·kg^{-1} when the thickness of sulfide SE layer was 50 μm, showing excellent application prospect [22]. Very recently, Meng's group reported a breakthrough in sulfide SE based prototype cells with Si anode via the carbon-free two-dimensional

---

Address correspondence to yingyinglu@zju.edu.cn

清华大学出版社 Tsinghua University Press Springer

structure design which can achieve a capacity retention of 80% after 500 cycles and an average columbic efficiency (CE) of > 99.9% at room temperature [23]. It indicates that ASSBs using sulfide SE and Si anode are becoming a new research hotspot of great scientific and commercial value. It is urgent and important to give a comprehensive review on sulfide SE and its application with Si anode.

In this review, we start with discussing the development history of sulfide SEs with high ionic conductivity in the context of the structural properties. We then emphasize the critical properties of sulfide SEs and the most recent improving strategies covering the air stability, electrochemical window, mechanical stability, thermostability and solvent stability. Later, we highlight the natural compatibility of Si anode to sulfide SEs. The main factors affecting the performance of ASSBs, including the carbon's effect, Si's particle size, pressure and sulfide' modules, Si's composite matrix and the depth of Si's lithiation, are elaborated in detail. Finally, we conclude by our perspective on the future development of high-performance ASSBs with sulfide SE and Si anode (Fig. 1). We hope this review can bring inspirations and provide reference for accelerating the research progress in this field.

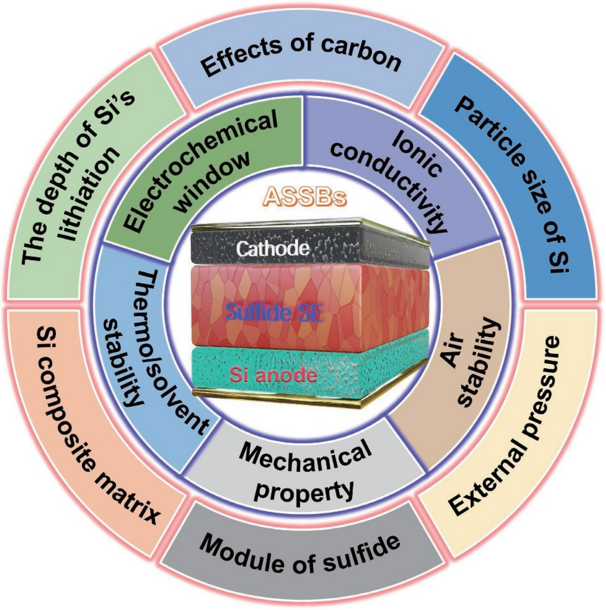

Figure 1 The application of sulfide SE and silicon anode in ASSBs. Bulk properties including electrochemical window, air stability, mechanical stability, thermostability and solvent stability are central to develop advanced sulfide SEs. The carbon's effect, Si's particle size, pressure and sulfide' modules, the depth of Si's lithiation and Si's composite matrix are the key factors to enable the application Si anode in sulfide SE-based ASSBs.

2 Sulfide electrolyte

2.1 History of sulfide electrolytes with high ionic conductivity

Ionic conductivity is the most essential property because it determines whether solid ionic conductors can be applied in ASSBs. The history to develop the categories of novel sulfide SEs is closely associated with improving this basic property. In general, sulfide SEs can be categorized into three types according to their structures: (1) thio-LISICON (LISICON = lithium superionic conductor), including $x\mathrm{Li_2S}$-$(1-x)\mathrm{P_2S_5}$ and $\mathrm{Li_{4-x}Ge_{1-x}P_xS_4}$ ($0 < x < 1$) which has a LISCON-structure originated from γ-$\mathrm{Li_3PO_4}$ [24, 25], (2) $\mathrm{Li_{11-x}M_{2-x}P_{1+x}S_{12}}$ (M = Ge, Si, Sn, etc.) derived from $\mathrm{Li_{10}GeP_2S_{12}}$ first developed by Kanno's group [26, 27] and (3) $\mathrm{Li_6PS_5X}$ (X = Cl, Br, I) derived from the mineral argyrodite ($\mathrm{Ag_8GeS_6}$) with an argyrodite structure [28, 29]. The room temperature ionic conductivity and the activation energy of typical sulfide SEs are summarized in Table 1.

Staring from the 1980s, the glassy materials such as $\mathrm{B_2S_3}$-$\mathrm{Li_2S}$-LiI, $\mathrm{Li_2S}$-$\mathrm{P_2S_5}$-LiI, and $\mathrm{Li_3PS_4}$ were explored (Figs. 2(a) and 2(b)), exhibiting an ionic conductivity of approximately 1 mS·cm^{-1} [32, 37]. The investigation of sulfide SEs slowed down because of the lost-competition in ionic conductivity with the rapid development and commercialization of organic liquid electrolyte based LIBs since the 1990s.

In the early 2000s, Tatsumisago's group systematically studied conductivity properties in $\mathrm{Li_2S}$-$\mathrm{P_2S_5}$ systems by controlling the compositions and heat treatment condition of $x\mathrm{Li_2S}$-$(1-x)\mathrm{P_2S_5}$ glasses [38]. They found the glass-ceramic sulfide SEs usually exhibited higher ionic conductivity than the glass or crystalline types. In 2005, the group identified the highly conductive $\mathrm{Li_7P_3S_{11}}$ phase in the 0.7$\mathrm{Li_2S}$-0.3$\mathrm{P_2S_5}$ system after annealing at 360 °C, which exhibits an outstanding ionic conductivity of 3.2 mS·cm^{-1} [39].

In 2008, the lithium argyrodites ($\mathrm{Li_6PS_5X}$, X = Cl, Br and I) were first revealed by Deiseroth's group with high ionic conductivity from 1 to 10 mS·cm^{-1} (Figs. 2(c) and 2(d)) [40]. Sylvain et al. synthesized a series of $\mathrm{Li_6PS_5X}$ (X = Cl, Br and I), in

Table 1 Ionic conductivity of typical sulfide-based solid electrolytes

Material	Ionic conductivity (S·cm^{-1})	Activation energy (eV)	Ref.
60$\mathrm{Li_2S}$-40$\mathrm{P_2S_5}$	3.2×10^{-6}	0.53	[30]
67$\mathrm{Li_2S}$-33$\mathrm{P_2S_5}$	3.8×10^{-5}	0.44	[30]
70$\mathrm{Li_2S}$-30$\mathrm{P_2S_5}$	3.7×10^{-5}	0.45	[30]
75$\mathrm{Li_2S}$-25$\mathrm{P_2S_5}$	2.8×10^{-4}	0.40	[30]
80(0.7$\mathrm{Li_2S}$-0.3$\mathrm{P_2S_5}$)-20LiI	5.6×10^{-4}	—	[31]
γ-$\mathrm{Li_3PS_4}$	3.0×10^{-7}	0.22	[32]
β-$\mathrm{Li_3PS_4}$	1.6×10^{-4}	0.16	[32]
$\mathrm{Li_7P_3S_{11}}$	1.7×10^{-2}	0.18	[33]
$\mathrm{Li_6PS_5Cl}$	1.3×10^{-3}	0.33	[34]
$\mathrm{Li_6PS_5I}$	6.3×10^{-4}	—	[28]
$\mathrm{Li_{10}GeP_2S_{12}}$	1.2×10^{-2}	0.21	[26]
$\mathrm{Li_{10}SnP_2S_{12}}$	4.0×10^{-3}	0.87	[35]
$\mathrm{Li_{9.54}Si_{1.74}P_{1.44}S_{11.7}Cl_{0.3}}$	2.5×10^{-2}	0.24	[36]

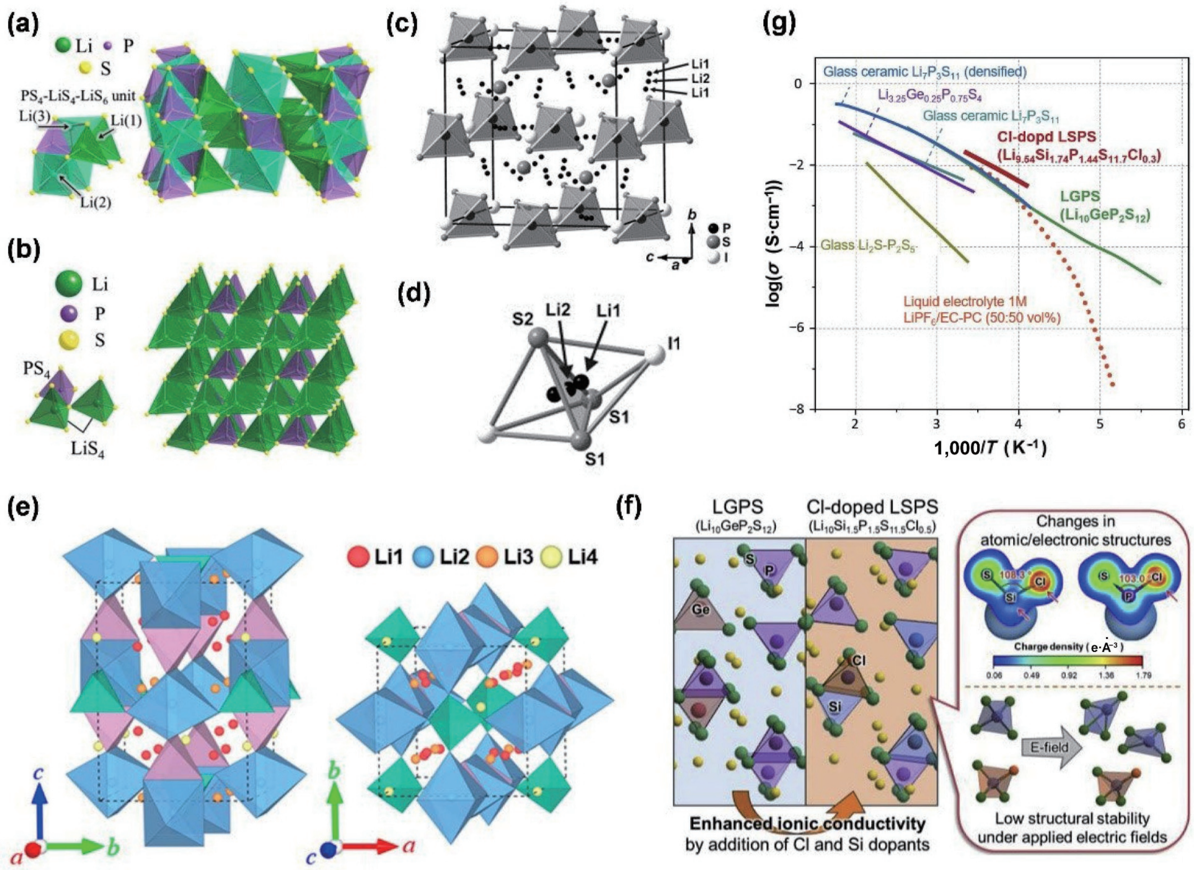

Figure 2 (a) Structure of β-Li_3PS_4. (b) Structure of γ-Li_3PS_4. (c) A section of the crystal structure of Li_6PSI_5 showing the distribution of PS_4 tetrahedra and single S^{2-}. (d) A face-sharing S_3I_2 double tetrahedron containing Li_1. (e) Framework structure of LGPS. (f) Illustration of crystal structure of $Li_{9.54}Si_{1.74}P_{1.44}S_{11.7}Cl_{0.3}$ and the enhanced ionic conductivity compared to LGPS. (g) Ionic conductivities of various sulfide-based SEs measured as a function of temperature. For comparison purposes, the ionic conductivity of a typical liquid electrolyte (1 M $LiPF_6$/EC-PC, 50:50 vol.%) is also shown as an orange dotted line. (a) and (b) Reproduced with permission from Ref. [37], © The Royal Society of Chemistry 2021. (c) and (d) Reproduced with permission from Ref. [40], © WILEY-VCH Verlag GmbH & Co. KGaA, Weinheim 2008. (e) Reproduced with permission from Ref. [27], © American Chemical Society 2018. (f) and (g) Reproduced with permission from Ref. [42], © Elsevier B. V. 2019.

which the Li_6PS_5Cl presented the highest ionic conductivity of 1.33 mS·cm⁻¹ [34]. Since then, the ionic conductivity of Li argyrodites were gradually improved by tuning the stoichiometric ratio and synthetic parameters. Recently, the ionic conductivity of Li_6PS_5Cl electrolyte was even increased to 10.2 mS·cm⁻¹ by an ultimate energy mechanical alloying synthesis method [41].

In 2011, the well-known superionic solid electrolyte $Li_{10}GeP_2S_{12}$ (LGPS) with three-dimensional (3D) framework structure was synthesized by the Kanno's group which showed a high ionic conductivity of 12 mS·cm⁻¹ (Fig. 2(e)) [26, 27]. The invention of LGPS, which signed that the conductivity of sulfide SEs began to overtake that of the conventional liquid electrolytes (about 10 mS·cm⁻¹), pushed the research of fast-ion conductors to climax and sparked great interest for studying ASSBs. In 2016, the same group cooperated with Toyota Motor Corporation reported a novel $Li_{9.54}Si_{1.74}P_{1.44}S_{11.7}Cl_{0.3}$ sulfide SE, displaying the highest ionic conductivity reported to date (25 mS·cm⁻¹) (Figs. 2(f) and 2(g)) [36, 42].

The ionic conductivity (σ) of sulfide SEs can be described by Arrennius equation: $\sigma = A\exp(-E_a/kT)$, in which A is the pre-exponential factor; E_a is the activation energy for lithium ion hopping through the SEs; T is the temperature in K; k is the Boltmann constant [43]. Based on the mathematical analysis, the sulfide SEs should have a considerable active lithium-ion concentration and low activation energy barrier for lithium ion transport in the inorganic framework. Typically, the former indicates a large number of mobile ions for conducting. The later calls for that the stable anion frameworks in SEs should have relatively open channels with plentiful available sites for the lithium-ion to migrate. For instance, Ceder's group revealed that body-centered cubic (bcc) anionic frameworks permitted direct hops between adjacent tetrahedral sites with lower activation energy while the tetrahedral-octahedral hops can be avoided (Figs. 3(a) and 3(b)) [44]. This bcc anionic framework is widely seen in fast ion conductors, such as $Li_7P_3S_{11}$ and LGPS. The group also used the structural matching algorithm to evaluate the similarity of typical structures containing Li and S to a bcc anion framework, where the angle deviation (σ_θ) and lattice length deviation (σ_l) should both be zero for an ideal compound with a perfect bcc anion framework (Fig. 3(c)). Indeed, the higher ionic conductivity of sulfide SEs roots in the lower electronegativity of sulfur atoms compared to oxygen atoms in oxide SEs so that the binding ability with lithium-ions is weaker, making lithium-ions more mobile in sulfide SEs. On the other hand, sulfur has a bigger atomic radius which can induce larger open channels for lithium-ion migration [45].

Based on these understandings, several strategies have been used to optimize sulfide SEs for achieving higher ionic conductivity. The most effective strategy is substitution or doping [46–48]. In general, high-valence cations are prone to create cation vacancies or anion interstitials for lithium-ion mobile. Besides, the arrangement of cations and anions in the SE's structural framework also plays the key role whose polyhedral structure exhibits a variety of possible coordination. The ions suitable for modification include Mo^{4+}, Si^{4+}, Ge^{4+}, N^{3-}, O^{2-}, F^-, and Cl^-, which have been well introduced by Zhou's review work [46]. Very

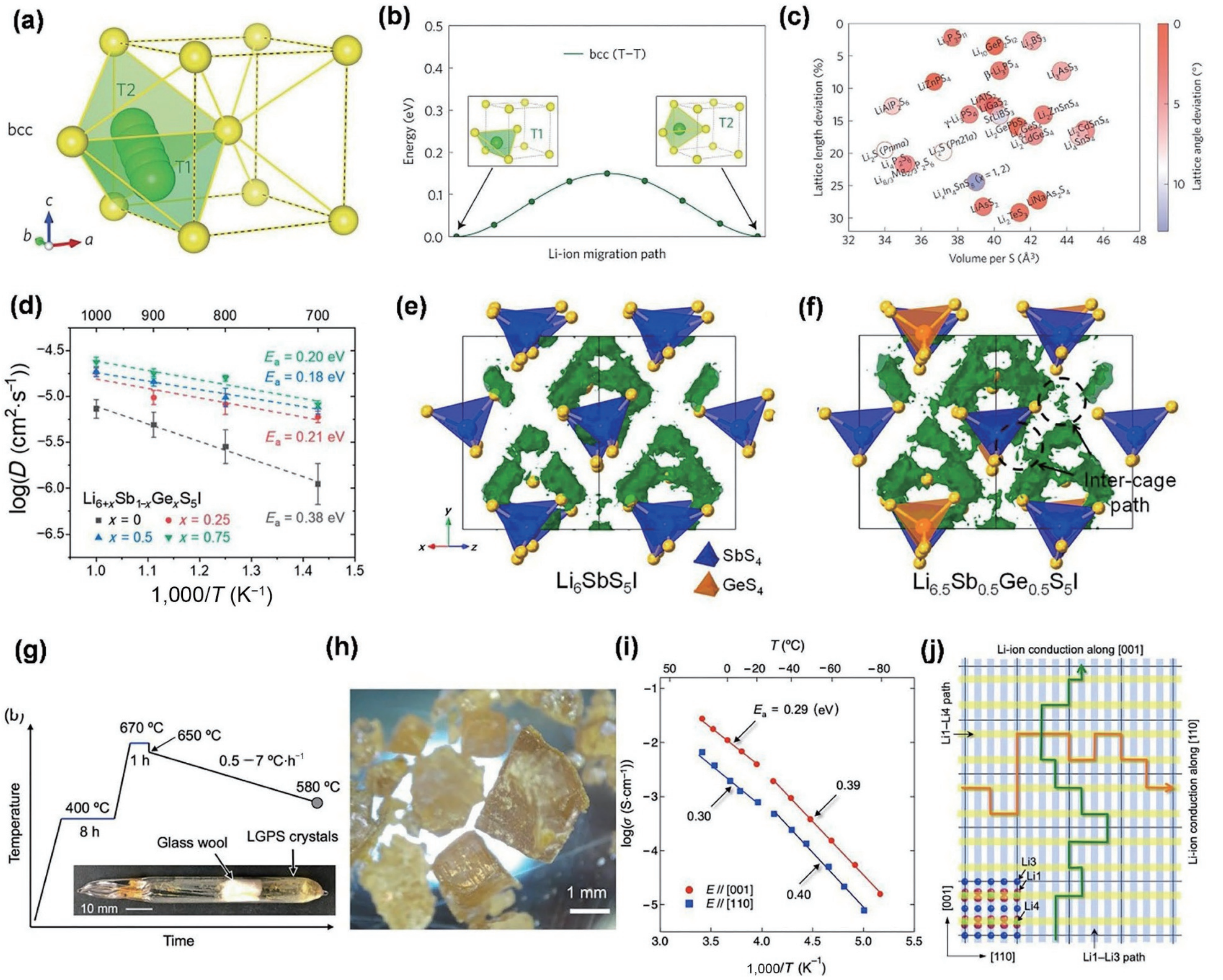

Figure 3 (a) Lithium-ion migration path in bcc structure. (b) The calculated energy path in bcc structure. (c) Similarity of screened structures containing Li and S to a bcc anion framework using the structural matching algorithm. For an ideal compound with a perfect bcc anion framework $\sigma_l = \sigma_\theta = 0$. (d) Arrhenius plots of lithium-ion diffusivity from *ab initio* molecular dynamic (AIMD) calculations for $Li_{6+x}Sb_{1-x}Ge_xS_5I$ (x = 0, 0.25, 0.5, and 0.75). (e) and (f) Isosurfaces of the lithium-ion probability densities (dark green) for (e) Li_6SbS_5I and (f) $Li_{6.5}Sb_{0.5}Ge_{0.5}S_5I$. (g) The synthesis process of LGPS single crystals. (h) The picture of the LGPS single crystals. (i) Arrhenius plots for the ionic conductivities in the [001] and [110] directions. (j) Schematic drawing illustrating the possible conducting paths of Li ions in LGPS. (a)–(c) Reproduced with permission from Ref. [44], © Macmillan Publishers Limited 2015. (d)–(f) Reproduced with permission from Ref. [49], © American Chemical Society 2021. (g)–(j) Reproduced with permission from Ref. [50], © American Chemical Society 2019.

recently, Yu's group synthesized Ge-substituted argyrodites $Li_{6.5}Sb_{0.5}Ge_{0.5}S_5I$ with an ionic conductivity of 16.1 mS·cm^{-1} (Fig. 3(d)) [49]. It demonstrated that concerted lithium-ion migrations through the inter-cage paths substantially increased the ionic conductivity (Figs. 3(e) and 3(f)). Besides, Tatsumisago's group reported that the ionic conductivity of heat-treated Li2S-P2S5 glass-ceramic conductor can be increased to 17 mS·cm^{-1} by reducing the grain-boundary resistance via a heat-treated procedure at 280 °C [33]. Recently, single crystals of the lithium-ion conductor LGPS have been successfully grown by the self-flux method based on the understanding of Li_4GeS_4-Li_3PS_4 pseudo-binary phase diagram (Figs. 3(g) and 3(h)) [50]. It was found that sulfide SEs with specific crystal plane orientation had higher ionic conductivity, e.g., 27 mS·cm^{-1} for single crystal LGPS along the (001) direction (Figs. 3(i) and 3(j)). It was also reported that mixing sulfide SEs with a small quantity of solid oxides, such as $Li_6ZnNb_4O_{14}$, Al_2O_3, or SiO_2, can also enhance ionic conductivity due to the "filler effect" [51]. These fundamental researches could help to further design the novel sulfide SEs with higher ionic conductivity.

2.2 Air stability derived from structural property of sulfide electrolytes

One of the main concerns with sulfide SEs is their poor chemical stability in air. Under ambient conditions, almost all sulfide materials undergo a hydrolysis reaction with moisture and generate H_2S gas, creating extremely ionic conductivity descend and potential safety hazards [52]. Usually, sulfide SEs must be operated in an environment filled with argon, which greatly increases the complexity and cost of the production. The air instability is originated from the sulfide's structural unit. The structures of sulfide SEs commonly involve repeated MS_4 tetrahedra units in which M refers to phosphorus or metal in Group 14 or 15, and S refers to sulfur [53]. The chemical formula of a typical category of sulfide materials thus can be noted as Li_4MS_4 (e.g., Li_4SnS_4) or Li_3M_S4 (e.g., Li_3PS_4). The aforementioned $Li_7P_3S_{11}$ phase with highest conductivity in $x$$Li_2S$-(1−$x$) P_2S_5 system owns one PS_4^{3-} unit, one pyrothiophosphate unit ($P_2S_7^{4-}$) and seven lithium ions to meat charge neutrality [39]. In argyrodite family (Li_6PS_5X, X = Cl, Br and I), the electrolyte structure is made up by one PS_4^{3-} unit, one S^{2-}, one halide ion and six lithium ions (Fig. 2(d)) [28, 29]. The structure of well-known LGPS consists of the GeS_4^{-} unit and two PS_4^{3-} units which are charged-balanced with ten lithium ions (Fig. 2(e)) [26]. The chemical instability of sulfide SEs with air is attributed to the vulnerability of the MS4 units. The M–S bonds in the MS_4 unit are easy to break and form a new bond with oxygen once exposure to moisture, because the M–O bond energy is quite larger than that of M–S bond. The decomposition reaction can be defined as $M_xS_y + H_2O \rightarrow M_xO_y + H_2S$ [24]. The air stability of the SEs can be identified by the amount of the generated H_2S gas after they expose to humid air, which are summarized in Table 2.

Based upon the structural analysis, when the stronger bond is formed in MS_4 unit, the sulfide SEs can exhibit improved air stability. With the same logic, hard-soft acid–base concept (HSAB) becomes the Bible to optimize the property [58, 59]. Based on HSAB, the metal elements in Group 14 or 15 (e.g., Sn^{4+}, Ge^{4+}, Sb^{5+} and As^{5+}) would form the stronger bond with sulfur than P^{5+}, because the former are much softer acids to bind with the soft S^{2-} base. A typical example is that the Li_4SnS_4 sulfide SE discovered by Kaib et al. exhibited greater air stability, though its ionic conductivity is only 0.07 $mS \cdot cm^{-1}$ [59]. Similarly, Li_3SbS_4 demonstrated fairly excellent air stability at the cost of ionic conductivity (approximately, 0.001 $mS \cdot cm^{-1}$) [54]. By contrast, the doping method is more useful. For instance, Sun's group reported that the addition of 7.5% Sb to LGPS as a dopant resulted in a minimal reduction of ionic conductivity from 17.3 to 15.7 $mS \cdot cm^{-1}$ even after exposing to air with 3% humidity for 24 h (Figs. 4(a) and 4(b)) [55]. However, in consideration of cost and energy density, the cation modified strategies should be avoided as possible, due to their high price (e.g., 25 $USD \cdot kg^{-1}$ for Sn vs. 2–3 $USD \cdot kg^{-1}$ for P) and density (e.g., 2.58 $g \cdot cm^{-3}$ for Li_4SnS_4 vs. 1.85 $g \cdot cm^{-3}$ for Li_3PS_4) [32, 59, 60]. In this case, oxygen or nitrogen substitution in SEs was developed to enhance their moisture stability. Tatsumisago's group reported that replacing S in Li_3PS_4 with a small amount of oxygen can enhance its moisture stability while negligibly influence the ionic conductivity [61].

Except for improving the air stability based on HSAB theory, alkali metal oxide absorption, physical isolation via core–shell nanostructure design or polymer hybrids, specific crystal plane exposure and super hydrophobic coating have been also developed. For the alkali metal oxide absorption, Tatsumisago's group illustrated that the metal oxides can role as an electrolyte additive for suppressing the evolution of H_2S gas [56]. The mechanism is that metal oxides such as ZnO, Fe_2O_3 and Bi_2O_3 have a large negative value of Gibbs energy change (△*G*) to react with H_2S. The composite electrolyte of $0.9Li_3PS_4$-0.1ZnO showed trace Li_2S release below 0.1 ppm with an ionic conductivity of 0.1 $mS \cdot cm^{-1}$. This design is consistent with the method commonly used in industrial production to remove H_2S from gas mixtures by

Table 2 Amounts of H_2S gas from different electrolytes in humid air ($cm^3 \cdot g^{-1}$)

Composition	Time exposure in air (min)	Amount of H_2S gas ($cm^3 \cdot g^{-1}$)	Ref.
$67Li_2S$-$33P_2S_5$	1	2.00	[24]
$80Li_2S$-$20P_2S_5$	1	0.60	[24]
$Li_7P_3S_{11}$	1	0.90	[24]
Li_3PS_4	1,000	38.00	[54]
Li_4SnS_4	1,000	5.00	[54]
Li_4SbS_4	950	1.00	[54]
$Li_{10}Ge(P_{0.925}Sb_{0.075})_2S_{12}$	1440	0.053	[55]
$90Li_3PS_4$-$10Fe_2O_3$	10	0.02	[56]
$90Li_3PS_4$-10ZnO	10	Almost 0	[56]
$90Li_3PS_4$-$10Bi_2O_3$	10	Almost 0	[56]
$Li_{3.06}P_{0.98}Zn_{0.02}S_{3.98}O_{0.02}$	180	0.0175	[57]

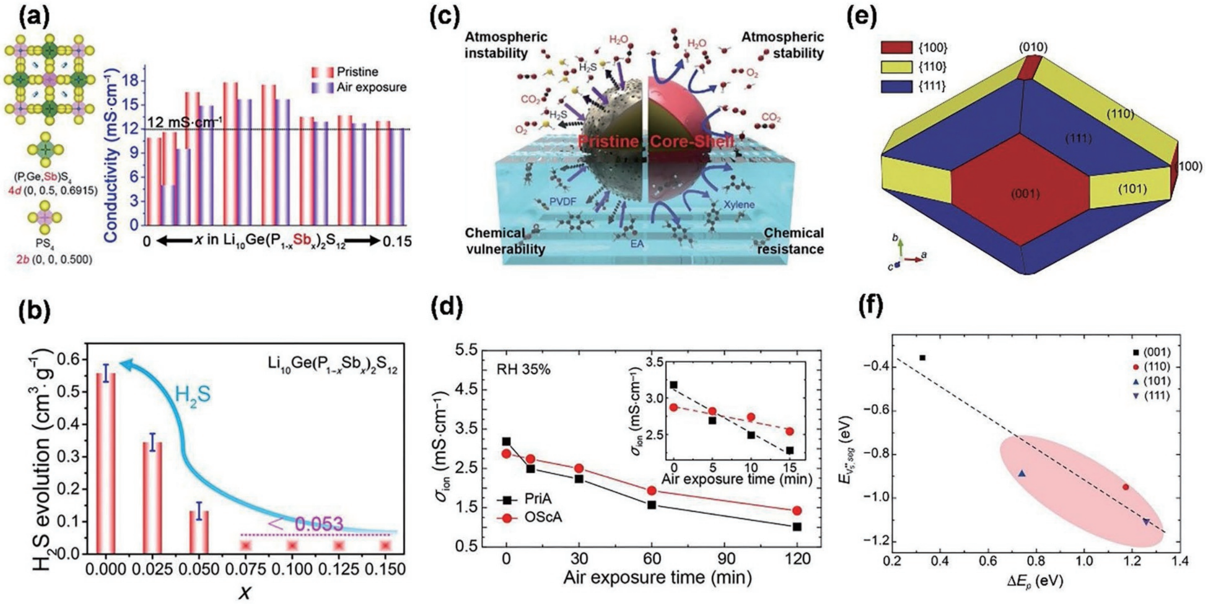

Figure 4 (a) The ionic conductivity of Sb-doped LGPS before and after air exposure. (b) Amount of H_2S gas generated from commercial LGPS and synthesized Sb doped LGPS powders. (c) Illustration of air stability and chemical vulnerability between pristine and core–shell SE particles. (d) Variations in ionic conductivity with ionic conductivity of SE with 35% relative humidity condition. (e) The predicted ECS of the β-Li_3PS_4 structure. (f) The relationship between $E_{VS^{\cdot\cdot}\text{seg}}$ and ΔE_p at the surface layer of each surface. (a) and (b) Reproduced with permission from Ref. [55], © American Chemical Society 2020. (c) and (d) Reproduced with permission from Ref. [62], © American Chemical Society 2020. (e) and (f) Reproduced with permission from Ref. [65], © Elsevier B. V. 2020.

ZnO absorbent. The alkali metal oxide absorption method is essentially a physical mixture between oxides and sulfide SEs. Recently, Xu' group introduced the Zn, O co-doping glass-ceramic Li_3PS_4 by adding 2% ZnO. The as-prepared sulfide material showed the excellent humid air tolerance as well as an improved conductivity of 1.12 mS·cm^{-1} [57]. The difference lies in the heat-treatment of the precursors at 250 °C to modify the materials structure to $Li_{3+3x}P_{1-x}Zn_xS_{4-x}O_x$.

As for physical isolation, the design principle is to use a functional nano-layer to coat the SE particles where the outer nano-layer does not block the lithium-ion diffusion among SE particles, resulting in both high ionic conductivity and good air stability. Kim's group used a post-oxidation process to build core–shell structured sulfide SEs with oxysulfide shells (Fig. 4(c)) [62]. The core–shell SEs exhibited good air stability for 30 min with an ionic conductivity of more than 2.5 mS·cm^{-1} (Fig. 4(d)). Besides, the compounds with polymers, such as 95 wt.% $Li_7P_3S_{11}$-5wt.%polystyrene-block-polyethylene-ran-butylene-block-polystyrene and 50 wt.% Li_3PS_4-50 wt.% poly(glycidyl methacrylate), were introduced to improve the sulfide's air stability [63, 64]. However, the introduction of polymers always decreases the lithium-ion diffusion path between sulfide particles, causing an ionic conductivity decline.

In the study of crystal planes, Kim's group used density functional theory (DFT) to analyze β-Li_3PS_4's surface structure and electronic properties [65]. They calculated the surface energy (φ) of 10 low refractive index surfaces of β-Li_3PS_4, and constructed the equilibrium crystal shape (ECS) of β-Li_3PS_4, which is a highly truncated octahedron (Fig. 4(e)). The group found that the (001), (111), (110) and (101) faces were the four stable crystal faces with low φ, while the (100) and (010) faces were much aggressive (Fig. 4(f)). Therefore, they proposed that the stability of sulfide SEs in air can be adjusted by controlling the exposed crystal plane during the synthesis.

Very recently, Wu's group first put forward the super hydrophobic interface in the fabrication of sulfide SEs [66]. The super hydrophobic protection layer consists of $Li_{1.4}Al_{0.4}Ti_{1.6}(PO_4)_3$ (LATP) nanoparticles as the lithium-ion conductive supporter and fluorinated polysiloxane (F-POS) via hydrolysis and condensation of tetraethyl orthosilicate and 1H,1H,2H,2H-perfluorodecyl triethoxysilane molecules as the super hydrophobic protagonist (Fig. 5(a)). The Li_6PS_5Cl SE was easily spray-coated with the F-POS@LATP composites by an airbrush, exhibiting excellent super hydrophobicity (water static contact angles > 160°) to resist extreme exposure even in the direct water jetting condition (Figs. 5(b) and 5(c)). The ASSBs using the extreme-condition-exposed modified Li_6PS_5Cl membrane exhibited a reversible capacity of 147.3 mAh·g^{-1}, almost same to the ASSBs using pristine sulfide SEs (Fig. 5(e)). The authors claimed that the super hydrophobic coating method was universal to protect all types of sulfide SEs from water (Fig. 5(d)). This work really inspires a lot as the exposure condition of this work is in harsh while the aforementioned modified strategies (HSAB, metal oxides absorption or physical isolation) are still limited to be tested in dry-room environment (< 3% relative humidity). However, the hydrophobic coating method must be applied after the bulk sulfide SEs have been fabricated in argon environment.

A one-step gas-phase synthesis method for sulfide SEs with raw materials in air, getting rid of the argon filled glovebox was reported by the Wu's group [67]. The investigators paid attention to the relative air-friendly L_4SnS_4 sulfide category and adjusted the base with substituted elements and concentrations. As a result, the As substituted $Li_{3.875}Sn_{0.875}As_{0.125}S_4$ materials exhibited air stability with the ionic conductivity of 2.45 mS·cm^{-1}. The pity is that the synthesized sulfide SE is costly with high mass density as mentioned above. Besides, the toxicity of some raw materials (e.g., CS_2 and As_2S_3) should not be ignored.

2.3 Electrochemical stability of sulfide electrolytes

Aside from the high ionic conductivity, a broad electrochemical

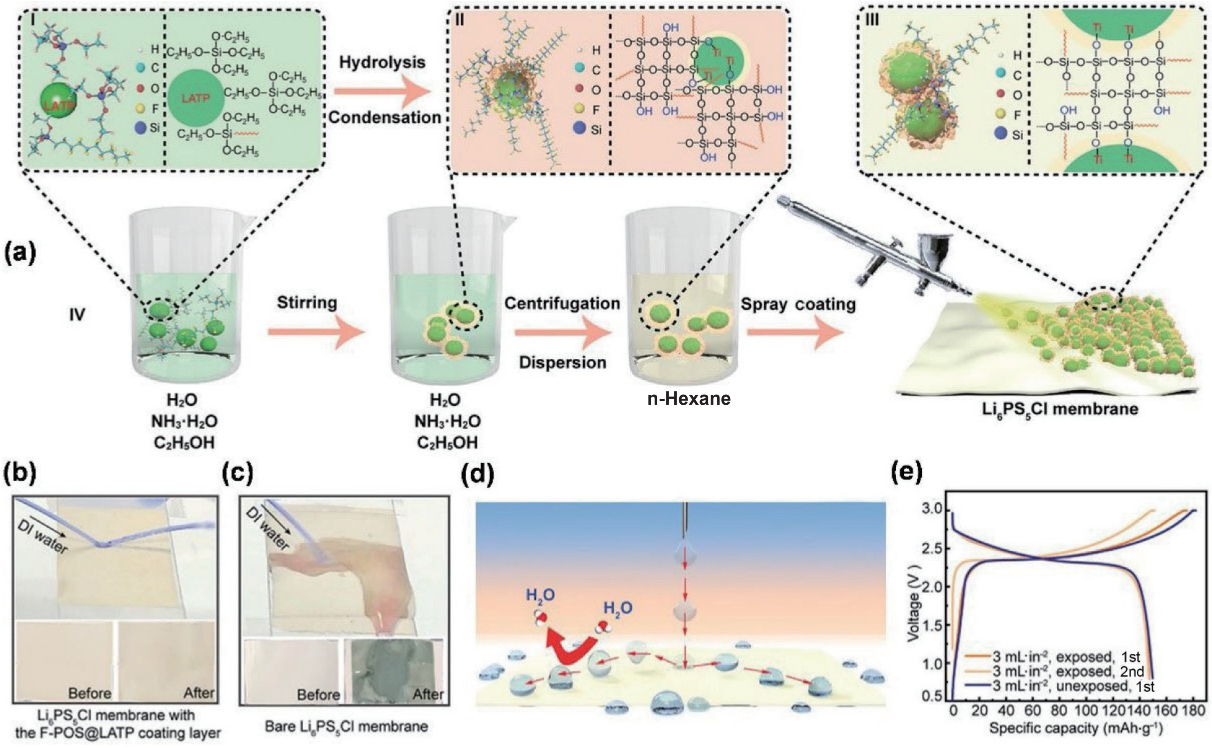

Figure 5 (a) Schematic illustrations of the preparation process of Li_6PS_5Cl SE spray-coated with the F-POS@LATP composites. (b) and (c) Photographs of (b) F-POS@LATP||Li_6PS_5Cl||F-POS@LATP membrane and (c) bare Li_6PS_5Cl membrane under, before, and after exposure water injection. (d) Schematic illustrations of F-POS@LATP||Li6PS5Cl||F-POS@LATP membrane under extreme exposure condition. (e) Charge/discharge profiles of LTO||Li_6PS_5Cl||LNO@LCO ASSBs using F-POS@LATP||Li_6PS_5Cl||F-POS@LATP membrane after exposure to the extreme condition. Reproduced with permission from Ref. [66], © Wiley-VCH GmbH 2021.

stability window is also a prerequisite to maximize the energy density of ASSBs. Electrolyte decomposition at the interface with high voltage cathodes (> 4.3 V vs. Li^+/Li) or low potential anode could both give rise to increased interfacial resistance and restrict the performance of the battery [68–70]. At the anode side, unlike the solid electrolyte interphase (SEI) passivation layer formed in organic liquid electrolytes, which is lithium ion conductive and electron-insulating, the SEI in sulfide ASSBs may be electronically conductive [69, 71]. For example, the soft cation included sulfide SEs (e.g., Li_4SnS_4 and LGPS) are susceptible to be reduced to generate Li alloys in SEI which will degrade the interfacial stability with even a risk of short circuit. As a result, an extra buffer layer is normally imperative between theses sulfide SEs and lithium metal anodes [72–75]. This demonstrates the advancement of silicon anode application, which will be mentioned in the following section.

As for high voltage tolerance, early works proposed that the most sulfide SEs had high potential stability with some SEs being stable up to 10 V vs. Li^+/Li [34, 45]. However, according to the work of Han et al., the early reported electrochemical stability window is often overestimated by the conventional experimental method using a lithium metal/electrolyte/inert metal semi-blocking electrode (Pt or stainless steel) because of the limited contact area and reaction kinetics between the sulfide SEs and inert metal [76]. As shown in Fig. 6(a), the stable electrochemical window of LGPS is only from 1.71 to 2.14 V vs. Li^+/Li based on theoretical calculation. They reported that adding carbon additives to enhance the contact area between SE and conductive agents was more reliable to evaluate the intrinsic electrochemical windows than traditional Li/electrolyte inert metal semi-blocking electrode. Using an in-house Li/electrolyte/SE-carbon cell setup, the authentic reduction and oxidation cyclic voltammetry (CV) identified the stable electrochemical window of LGPS was from 1.7 to 2.1 V vs. Li^+/Li (Figs. 6(b) and 6(c)).

Mo’s group calculated the lithium chemical potential and energy of phase equilibria at applied voltage using DFT method. They demonstrated that the intrinsic electrochemical window of the common SEs was determined by the thermodynamically favorable decomposition products (Figs. 6(d) and 6(e)) [77]. Nevertheless, evaluation of the electrochemical stability by Mo’s group based on differences in formation energies, indeed leads to much narrower electrochemical windows compared to those in practice. The reason for this is that thermodynamic evaluations do not take into account the kinetic barriers of decomposition reactions. Very recently, Wagemaker’s group reported that the most favorable decomposition pathway for the argyrodite Li_6PS_5Cl was indirect lithiation, rather than direct decomposition to the most thermodynamically stable decomposition species [78]. They

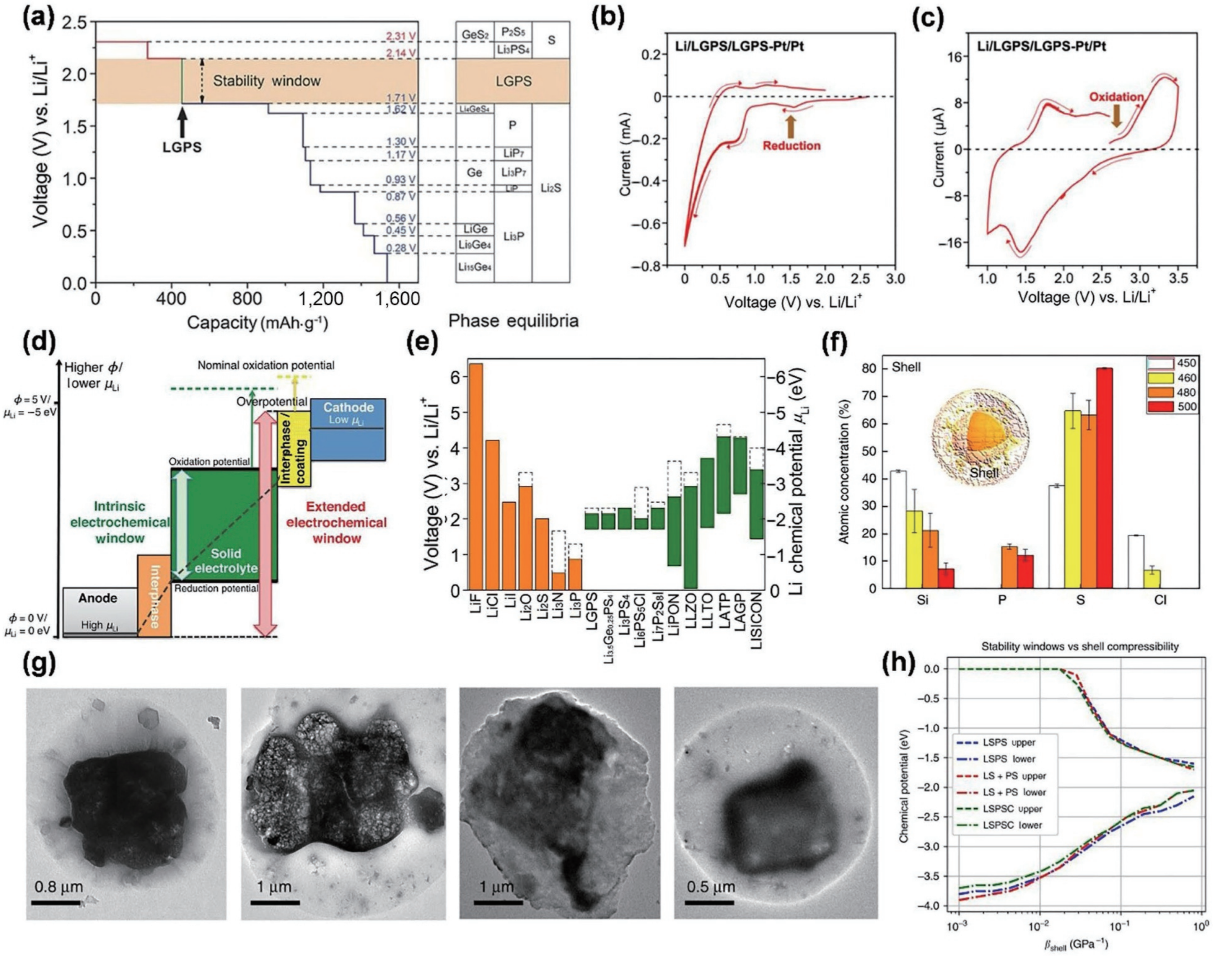

Figure 6 (a) The first-principles calculation results of the voltage profile and phase equilibrium of LGPS solid electrolyte upon lithiation and delithiation. (b) and (c) Cyclic voltammetry of Li||LGPS-Pt||Pt semi-blocking electrode at a scan rate of 0.1 $mV\cdot s^{-1}$ in the voltage range of (b) 0–2.0 V and (c) 1.0–3.5 V. (d) Schematic diagram about the electrochemical window (color bars) and the Li chemical potential profile (black line) in the ASSBs. (e) Electrochemical window (solid color bar) of solid electrolyte and other materials. (f) Scanning transmission electron microscopy (STEM) EDS analyses of the samples showing the shell–core structure versus the increasing annealing temperature. (g) TEM images of core–shell structured $Li_{9.54}Si_{1.74}P_{1.44}S_{11.7}Cl_{0.3}$ annealed at 450, 460, 480, and 500°C, respectively. (h) Stability windows for SEs as a function of shell effective compressibility. (a)–(c) Reproduced with permission from Ref. [76], © WILEY-VCH Verlag GmbH & Co. KGaA, Weinheim 2016. (d) and (e) Reproduced with permission from Ref. [77], © American Chemical Society 2015. (f)–(h) Reproduced with permission from Ref. [82], © Wu, F. et al. 2018.

revealed that the reduction and oxidation voltage of Li_6PS_5Cl occurred at 1.08 and 2.24 V vs. Li^+/Li, respectively, which agrees well with the accurate electrochemical measurements and makes up for Mo's calculation. Based on the continuously optimized calculation theory, we believe that the calculation method can provide a reference for designing and optimizing electrolytes with wider electrochemical stability.

Composition tuning, morphological control and interface modification are promising approaches to improve the electrochemical stability of sulfide SEs. Zhang et al. reported that the O-doped Li_6PS_5Br argyrodite could suppress the side reaction with the lithium anode and showed improved cycling performance with high-voltage $LiCoO_2$ cathode [79]. The fabricated $Li_6PS_{4.7}O_{0.3}Br$ ASSBs could cycle steadily over 900 cycles at a higher current density of 0.4 $mA\cdot cm^{-2}$. By contrast, the bare Li_6PS_5Br short-circuited only after 560 cycles at a lower current density of 0.1 $mA\cdot cm^{-2}$. They proposed the O atoms preferred to occupy the free S^{2-} sites rather than PS_4 tetrahedra unit, enabling better electrochemical stability. Kanno's group also illustrated that the O doping $Li_{9.42}Si_{1.02}P_{2.1}O_{2.01}$ (LSiPSO) could exhibit improved compatibility with lithium anode [80]. Chen's group developed an Al^{3+} cations doped sulfide SE ($Li_{11}AlP_2S_{12}$) which shares a similar thio-LISICON structure with the LGPS, showing enhanced electrochemical stability higher than 5 V vs. Li^+/Li [81]. As for morphological control, a special core–shell structure was built by Wu et al, where a single crystalline $Li_{9.54}Si_{1.74}P_{1.44}S_{11.7}Cl_{0.3}$ core was enclosed by an amorphous shell (Fig. 6(f)) [82]. The electrochemical window of the SE could be broadened to 0.7–3.1 V vs. Li^+/Li and showed a quasi-stability window upwards 5 V vs. Li^+/Li, which is much larger than the reported 1.7–2.1 V vs. Li^+/Li. The researchers found higher Si content could appear in the shell, generating much stronger mechanical compressibility to the core when the materials were treated at lower temperature (Fig. 6(g)). The improved voltage window could be attributed to the volume constriction under the enhanced mechanical compressibility, which resists the decomposition reaction of the sulfide SE (Fig. 6(h)). This research emphasized the opportunity of mechanical passivation of the electrolyte materials by microstructural design. Surface engineering of sulfide SEs could also improve the electrochemical stabilities. Meng et al. summarized the recent advances of atomic and molecular layer deposition (ALD and MLD) to modify the electrode–SE interface with improved electrochemical stability and interfacial contact [83, 84]. In addition, it is reported that the coating layers on high voltage cathodes could seclude the sulfide SEs from the low lithium chemical potentials exerted by the cathode particle in its charged state so that the oxidation as well as the delithiation of sulfide SEs at the interface will be suppressed [85–88]. $LiNbO_3$, $LiPO_4$, $Li_4Ti_5O_{12}$ and Li_2O-ZrO_2 (LZO) are the most popular coating materials which could be applied on the surface of high voltage cathode particles to hinder the unfavorable side reactions. Yao's group reported that the Li_6PS_5Cl sulfide SE could tolerate the 5 V-class spinel $LiNi_{0.5}Mn_{1.5}O_4$ (LNMO) cathode coated with 8 wt.% $LiNbO_3$ [86]. Haruyama et al. proposed that the improved high voltage electrochemical stability was attributed to the inhibited interfacial space charge effect as the $LiNbO_3$ buffer layer formed smooth interfaces without Li adsorption sites for both sulfide and high voltage cathodes [85].

2.4 Mechanical property of sulfide electrolytes

The mechanical stability of sulfide SEs is critical in evaluating their viability in the interfacial compatibility with electrodes and fabrication process. During the operation, significant mechanical stresses would develop in ASSBs because of the volume changes of the electrode active materials upon lithiation/delithiation. Using the *in-situ* pressure measurements, Zhang et al. found that the ASSBs could undergo a "breathing" phenomenon with a periodic pressure fluctuated by up to 1.25 MPa in each cycle [89]. Thus, the interfacial contact could be lost, leading to capacity loss. More importantly, the electrochemical strain may result in large local stress and induce the crack formation and even the particle deformation [90]. SEs with low elastic moduli can relax the large mechanical stresses and confer more stable cycling of ASSBs. In general, sulfide materials are much ductile than the oxides. For example, the Young's moduli of Li_2S-P_2S_5 glasses are about 18–25 GPa while the $Li_7La_3Zr_2O_{12}$ which is normally used as the oxide SE has much large moduli of about 150 GPa [91, 92]. The mechanical properties of sulfide SEs are usually measured by acoustic measurements and indentation experiments in a fluid cell [93, 94]. The ductile nature of sulfide materials can be attributed to the lack of periodic, long-range ordering and the presence of free volume/dangling bonds. To release the mechanical stress derived from the volume change of active electrode particles, the "zero-strain" electrode was reported by Janek's group [95]. They experimentally demonstrated that cathode composite with negative volume expansion $Li(Ni_{1-x-y}Co_xMn_y)O_2$ and positive volume expansion $LiCoO_2$ in a weight ratio of 55: 45, could significantly mitigate the volume strains and provide excellent contact with ionic conduction pathways in ASSBs.

The low elastic modulus of sulfide SEs allows for a cold-pressing process to reduce the grain boundary resistances for better battery performance. Typically, cathode and anode active materials are hand-milled with conductive additive and sulfide SE particles to ensure good electronic and ionic conductivity. Then, the composites are cold-pressed into electrode pellets, respectively. The two electrodes are finally separated by a SE pellet in a stack and cold-pressed again into a mold cell for testing under an extra pressure [96]. The pressure ensures the good interfacial contact between sulfide-sulfide and sulfide-electrodes. It was reported that a pressure of 360 MPa could significantly densify $0.75Li_2S$-$0.25P_2S_5$, showing the improved ionic conductivity by nearly one order compared with that in 70 MPa [97]. By contrast, the pressure of 360 MPa made the stiffer $Li_7La_3Zr_2O_{12}$ little densification with an ionic conductivity too low to measure [91, 93]. Except for ionic conductivity, it is also reported that the electrochemical window could be considerably widened from 1.7–2.1 V vs. Li^+/Li to 0.495 V to 2.5 V vs. Li^+/Li with a larger applied pressure of 20 GPa [82]. However, the huge applied pressure could damage the mold and is impractical for its commercialization.

Cold-pressed sulfide SE pellets often have considerable porosity of 25%–28%. Filling the empty voids of sulfide particles with organic polymers, the composite electrolyte could achieve higher mechanical flexibility with proper ionic conductivity. Liu's group developed composite SEs consisting of $0.4GeS_2$-$0.3Li_2S$-$0.3LiI$ glass and 13 vol.% PEO polymer with lithium bis (trifluoromethane) sulfonimide (LiTFSI) salt as the additive [98]. The interfacial resistance of the composite SE-electrode remained constant at 80 °C for 250 h, demonstrating the improved interfacial contact. Lee's group developed an *in-situ* crosslinking process to construct a continuous network in $0.775Li_2S$-$0.225P_2S_5$ sulfide SEs by introducing 20% polyimine polymers, along with the heating and pressing process [99]. The void spaces in the sulfide SE were ideally filled by the polyimine, significantly improving the malleable property and mechanical stability of the composite SE. Moreover, the SE membrane achieved an ultrathin thickness of 63.7 μm without obvious fracture, attributed to the excellent dispersion and connected domains of flexible polyimine. Jung's group reported a thin and bendable sulfide composite SE (Li_3PS_4 and LGPS) membrane based on a mechanically flexible poly-

(paraphenylene terephthalamide) (PPTA) nonwoven (NW) scaffold (Fig. 7(a)) [100]. The composite has an ionic conductivity of 0.2 mS·cm^{-1} at 30 °C with a thickness of 70 μm (Fig. 7(b)). The bendability of the composite film is originated from the high flexibility of the polymer, ensuring the mechanical integrity of the SE and preventing fracture on account of structural pores or defects (Fig. 7(c)). The ASSB, using a thin NW-reinforced SE film, delivers the increase of the cell-energy-density compared to that of a conventional cell without the NW scaffold (Fig. 7(d)). However, the improved mechanical stability of polymer-sulfide composite design is at the expense of the decreased ionic conductivity due to the covering of fast ion conductive sulfide's surface. Effectively improving the ionic conductivity of the polymer/inorganic composite SE to greater than 1 mS·cm^{-1} at room temperature is one of the key problems. Very recently, Sun's group reported the inorganic SEs freestanding films interweaved by polytetrafluoroethylene (PTFE) (Fig. 7(e)) [101]. The fabrication method could be universal for Li_6PS_5Cl, Li_3InCl_6, and $Li_{6.5}La_3Zr_{1.5}Ta_{0.5}O_{12}$, showing not only an ultrathin thickness of 15–20 μm comparable to that of the conventional polymeric separators (Fig. 7(f)), but also high room-temperature ionic conductivity of more than 1 mS·cm^{-1} (Fig. 7(g)). The high ionic conductivity of the fabricated SEs could be originated from the solvent-free process and a small amount of PTFE additive (< 0.5%) benefiting its high tensile strength. As a result, practical pouch type ASSBs with sulfide SE delivered a high specific capacity of 124.3 mAh·g^{-1} at 0.1 C with the exceptional cycling stability (Figs. 7(h) and 7(i)).

2.5 The synthesis methods according to sulfide's thermal and solvent stability

The thermal and solvent stability of sulfide SEs could exert a tremendous influence in the synthesis process. Temperature significantly affects the purity of the fast ionic conductor phase. In LGPS, recent research based on temperature-dependent X-ray diffraction (XRD) revealed the formation of the $Li_4P_2S_6$ impurity phase between 300 and 400 °C [102, 103]. The $Li_4P_2S_6$ phase with inadequate ionic conductivity (0.0023 mS·cm^{-1}) could lead to a substantially lower ionic conductivity for the LGPS. The $Li_7P_3S_{11}$ fast lithium ion conductive SE also shows the similar issue, where the impurity phase $Li_4P_2S_6$ could precipitate at 300 °C, significantly decreasing the overall ionic conductivity [104]. In the xLi$_2$S-(1−x) P$_2$S$_5$ system, the earliest synthesized product γ-Li_3PS_4 which can be dated back to 1984 displayed a low ionic conductivity of 10^{-4} mS·cm^{-1}. When heated to 195 °C, the γ-Li_3PS_4 is converted to the highly conductive β-Li_3PS_4 phase with an ionic conductivity of about 10^{-1} mS·cm^{-1} [105]. Further increasing the temperature to more than 485 °C could result in the α-Li_3PS_4, once again lowering the conductivity [32]. In addition, the β-Li_3PS_4 is meta-stable and easily reverts to the stable γ-Li_3PS_4 phase at the temperature below 195 °C. As a result, stabilizing the high purity of conductive β-Li_3PS_4 at room temperature is with challenge. The poor thermos-stability of sulfide SEs at higher temperature needs that the hot-pressing temperature should not be too high (below 300 °C as possible) if the densification process is necessary, and the synthetic temperature should match the stability of the related SEs.

Solid-state route and mechanical ball-milling route are

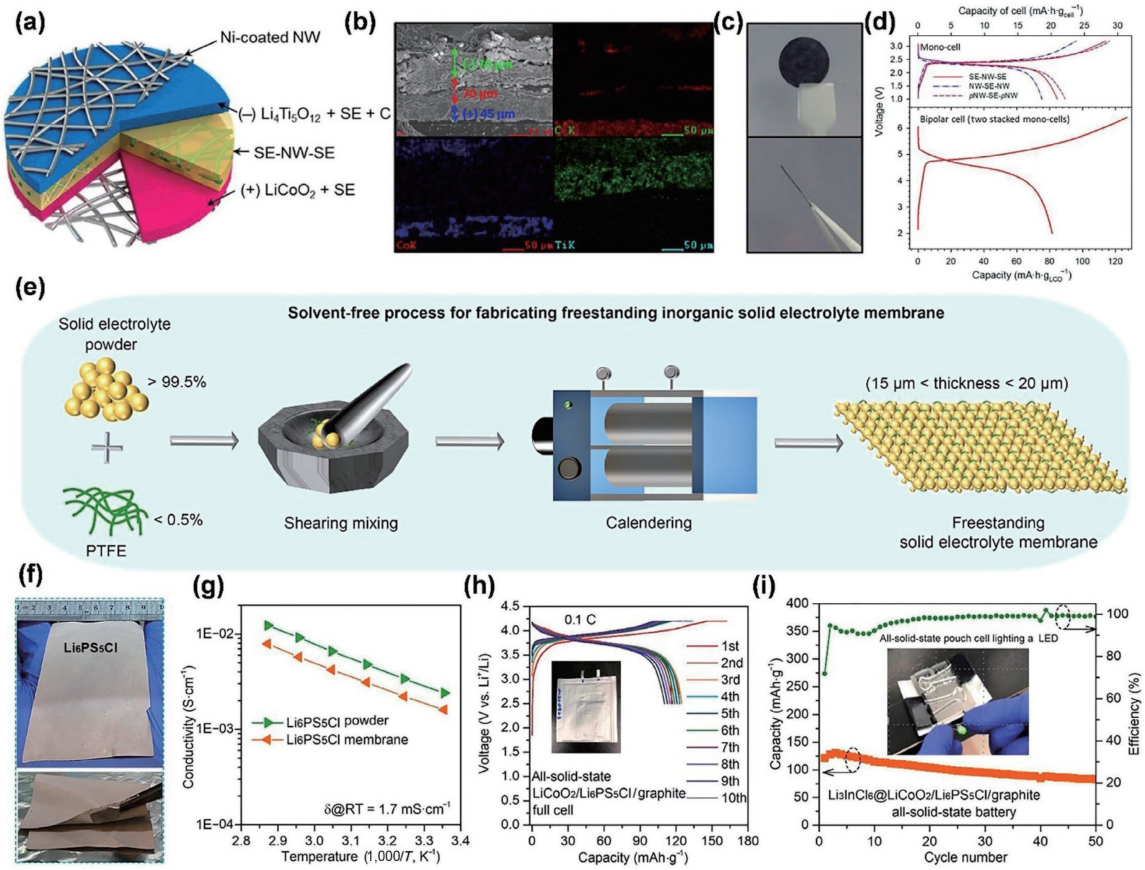

Figure 7 (a) Schematic diagram of the mechanically flexible PPTA NW scaffold. (b) Cross-sectional field emission scanning electron microscopy (FESEM) image and EDS elemental maps. (c) Photo images of the free-standing $LiCoO_2$||(SE-NW-SE)||$Li_4Ti_5O_{12}$ fabrication. (d) First charge–discharge voltage profiles of the free-standing $LiCoO_2/Li_4Ti_5O_{12}$ all-solid-state mono-cells with different-structured SE films and the free-standing bipolar cell constructed by stacking two free-standing mono-cells. (e) Schematic of the fabrication process for thin PTFE-based SE membranes. (f) Photos of the PTFE-based Li_6PS_5Cl. (g) Arrhenius plot of Li_6PS_5Cl powder and its membrane. (h) Initial 10 charge–discharge curves of Li_6PS_5Cl membrane-based ASSBs. (i) The cycling stability at room temperature. (a)–(d) Reproduced with permission from Ref. [100], © American Chemical Society 2015. (e)–(i) Reproduced with permission from Ref. [101], © American Chemical Society 2021.

commonly used to synthesize the sulfide materials. The solid state reaction requires the adequate solid–solid particles contact so that the high temperature is necessary for improving the kinetics of the reaction. The high temperature would potentially increase the risk of impurity products due to the interaction between the reaction regents and the reaction vessel, and the poor thermos-stability of the sulfides [32, 105]. Moreover, the high temperature solid-state route should use the evacuated carbon-coated quartz tubes to prevent the release of sulfur species with high vapor pressure and suppress the side reaction between materials and reaction vessels, indicating the scale-up of such synthetic approaches impracticable [25, 106]. Though the mechanical route could enhance the kinetics of reaction from the high-energy ball-milling at room temperature, it is also reported contamination such as $Li_4P_2S_6$ could not be prevented, because all the collisions and friction in the jar during the ball-milling operation generate heat to induce the side reaction [30]. In addition, it is also noted that the ionic conductivity of the mechanical synthesized sulfide glass-ceramics is intensively dependent on the subsequent high-temperature annealing process, making the temperature control challenging [107, 108].

Liquid-phase synthesis has been proposed for the production of sulfide materials, involving the reaction of reagents in solvent medium and the subsequent purification of the compound of interest [109]. The stability of sulfide SEs against organic solvents plays the decisive role to promote the scale-up of the liquid-phase routes. Chen's group isolated various $Li_7P_3S_{11}$-solvent systems and studied their molecular level interactions by combining various characterization tools (Figs. 8(b) and 8(c)) [60]. In their study, various color changes were observed, as seen in Fig. 8(a), where N-methyl-2-pyrrolidone (NMP) and dimethylformamide (DMF) solutions turned dark green and blue, respectively, and methyl ethyl ketone (MEK) solutions turned yellow initially before settling to a yellowish-white color, indicating chemical degradation of $Li_7P_3S_{11}$ when exposed to these solvents. Typically, the organic solvents should be aprotic to avoid protonation of the sulfide ion, which would result in SH^- or $H_xPS_4^{3-x}$ impurities as well as hazardous H_2S gas. Additionally, the solvents that have proven successful are (at least substantially) polar, emphasizing the solvent molecules' active role in facilitating the process. Based upon the consideration, tetrahydrofuran (THF), acetonitrile (ACN), 1,2-dimethoxyethane (DME), ethyl acetate (EA), dimethyl carbonate

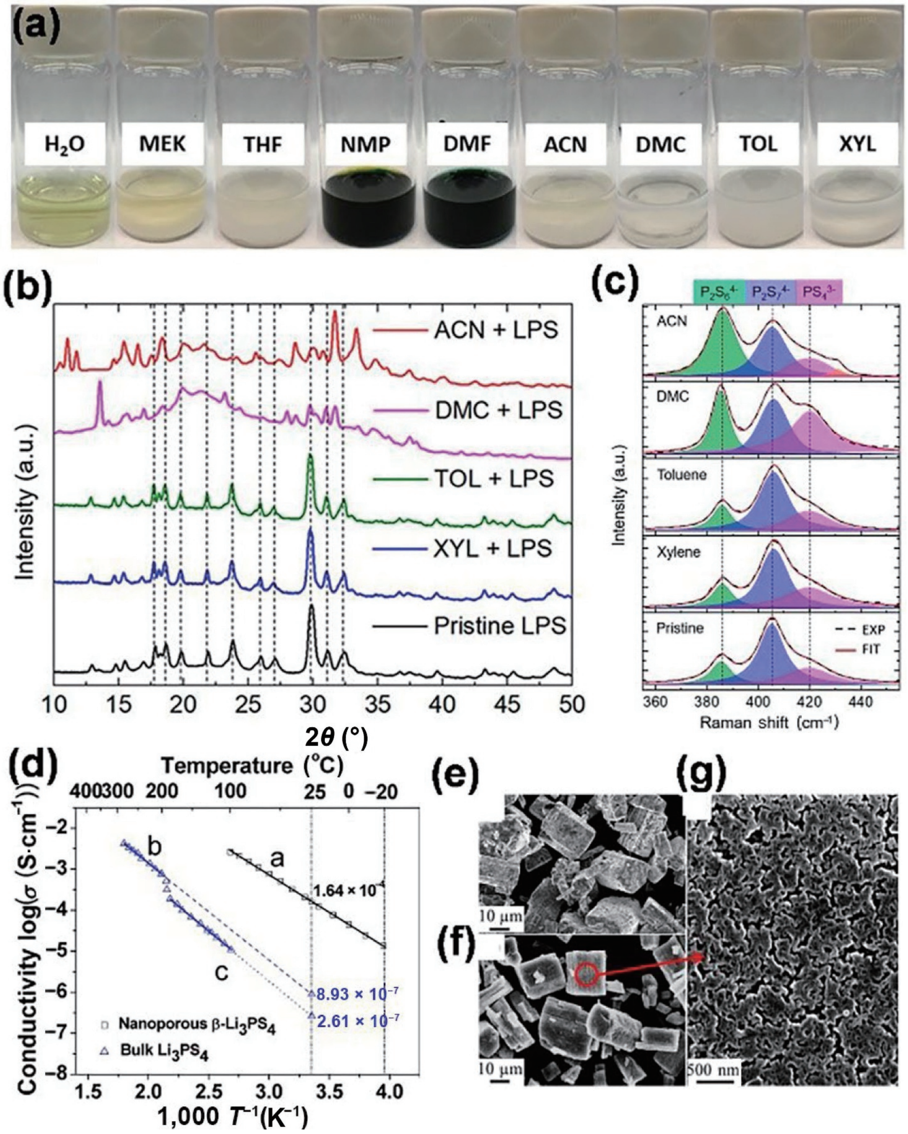

Figure 8 (a) Different solvent color changes after addition of $Li_7P_3S_{11}$. (b) XRD patterns of $Li_7P_3S_{11}$ after dispersion in ACN, DMC, toluene (TOL), and p-xylene (XYL). (c) Raman spectra of $Li_7P_3S_{11}$ after dispersion in different solvents. (d) Arrhenius plots for nanoporous β-Li_3PS_4 (line a), bulk β-Li_3PS_4 (line b), and bulk γ-Li_3PS_4 (line c). (e) Morphology of as-synthesized Li_3PS_4·3THF particles. (f) Morphology of nanoporous β-Li_3PS_4 particles. (g) Surface of the nanoporous β-Li_3PS_4. (a)–(c) Reproduced with permission from Ref. [64], © American Chemical Society 2019. (d)–(g) Reproduced with permission from Ref. [118], © American Chemical Society 2013.

(DMC) and ethyl propionate (EP) are the common polar aprotic solvents used in the production of sulfide SEs [110–116].

The temperature in the liquid-phase synthesis route is typically below 300 °C which is much lower than that in the solid-state route (commonly above 500 °C), thus avoiding the possible formation of impurities [117]. The liquid-phase reaction is often at room temperature and the heat treatment is mainly applied in the purification process in which the solvent molecules need to be removed to obtain the pure sulfide materials. The purification process is usually performed by heating the precipitation compounds under vacuum and the temperature is decided by the volatility of the solvent (e.g., 80 °C for THF and 250 °C for DME). In 2013, Liang's group reported the production of β-Li_3PS_4 by liquid-phase synthesis [118]. The Li_3PS_4-3THF complex was formed after overnight stirring of Li_2S and P_2S_5 in THF and the subsequent centrifugation. This compound was further heated at 80 °C under vacuum to remove the co-crystallized solvent, resulting in the creation of amorphous Li_3PS_4 with an ionic conductivity of 7.4×10^{-2} mS·cm^{-1} (Fig. 8(d)). Nano-porous β-Li_3PS_4 with high ionic conductivity of 1.6×10^{-1} mS·cm^{-1} could be finally formed after heating at 140 °C. It indicates that the liquid-phase synthesis could lead to the thermodynamically metastable phase at low temperature. Moreover, the produced powders were submicrometres to a few micrometres in size and had very porous architectures, making them ideal for cold or warm sintering to produce dense membranes (Figs. 8(e)–8(g)). In 2014, the same group reported employing ACN to create a new phase, $Li_7P_2S_8I$, by the liquid-phase route, suggesting that the liquid route could be performed to explore novel sulfide materials [28]. The synthesis consisted of forming a Li_3PS_4-2ACN complex in the ACN solvent after stirring for 24 h, then combining this complex with LiI in ACN, and finally heating at 200 °C to remove the co-crystallized ACN. The as-synthesized $Li_7P_2S_8I$ had a good stability towards metallic lithium with an ionic conductivity of 6.3×10^{-1} mS·cm^{-1}. Although the liquid-phase route can be used to synthesize the meta-stable β-Li_3PS_4 or $Li_7P_3S_{11}$ with desirable ionic conductivity at room temperature, avoiding the possible impurities, the conductivities of other sulfide materials are often lower than those gained by solid-state routes [109]. For example, most Li_6PS_5X (X = Cl, Br, I) argyrodite synthesized by liquid methods and heating below 300 °C showed the ionic conductivities of 10^{-2}–10^{-1} mS·cm^{-1}, which were at least one order of magnitude lower than those of electrolytes performed by solid-state process (about 1 mS·cm^{-1}) [34, 119]. Very recently, Lee et al. reported the first universal solution synthesis of sulfides using an alkahest solvent system [120]. The binary mixture solvent of 1,2-ethylenediamine (EDA) and 1,2-ethanedithiol (EDT) (or ethanethiol) can not only effectively dissolve the conventional sulfide SE precursors of Li_2S, P_2S_5, LiCl, but also insoluble metal sulfides, such as GeS_2 and SnS_2. The homogeneous solution synthesis has multiple advantages, such as reduced reaction time and scalable production of SEs compared to the suspension synthesis process using DME or ACN solvent. Raman spectroscopy revealed that the extraordinary dissolving capability of EDA-EDT toward the GeS_2 was owing to the nucleophilicity of the thiolate anions, which is powerful enough to break the Ge–S bonds. The targeted LGPS and Li_6PS_5Cl (LPSCl) SEs with ionic conductivities of 0.74 and 1.3 mS·cm^{-1}, respectively, were obtained by dissolving related precursors in EDA-EDT solvents, followed by evaporating the solvent via high temperature treatment of 700 °C. The ionic conductivities are still much lower than those of the SEs synthesized by a solid-state method and the excessive temperature limits the method.

Despite the recent success of such wet chemical approaches, the reaction mechanism between the reagents in liquid solvents is not yet well understood. It should also be noted that no investigation has demonstrated conductivities higher than 1 mS·cm^{-1} utilizing heating temperatures below 300 °C, suggesting that the different solvents, additives, and mixing tactics, as well as the solvent-to-reagent ratio and drying procedure, should be optimized further.

3 All-solid-state batteries with silicon anode

3.1 Anode material options

In Section 2, we have reviewed the development history and typical bulk properties as well as the related modification strategies of sulfide SEs. To achieve high-energy density ASSBs for practical use, both ideal anode and cathode should be performed with high specific capacity and proper potential, of which the anode should own the lower electrochemical potential and the cathode should own the opposite (Fig. 6(d)) [3, 68, 121]. Interfacial instability thus becomes another challenging obstacle due to the intensified interfacial reactions. Recently, Fan's group has particularly introduced the current status and future directions of sulfide SEs with the star cathodes, such as high voltage $LiCoO_2$ or Ni-rich $LiNi_{0.8}Co_{0.1}Mn_{0.1}O_2$ (NCM811) [122], so we would not tautologically discuss the cathodes in this review.

For the anode choice, indium (In) and the alloy of In with Li are currently the most employed anodes in sulfide SE-based ASSBs due to their excellent stability with sulfide and constant electrochemical potential [123, 124]. However, the heavy density (7.31 g·cm^{-3}) and high cost (150 k\$·ton^{-1}) of In make them challenging to be used in industrial applications. Moreover, the high reduction potential of ~ 0.62 V (vs. Li^+/Li) hinders the development of high-energy density ASSBs by decreasing the battery's output voltage [125]. It demonstrates that the In or the alloy of In with the Li anode are only suitable to evaluate the sulfide SE's performance or the compatibility of the SE and cathode. In addition, commercial graphite anode is criticized for its low specific capacity (372 mAh·g^{-1}). As a result, tremendous efforts are being made to find other promising anode candidates, including conversion, alloy, and intercalation types [126]. Among them, lithium metal and silicon are two of the most attractive anode materials because of their ultrahigh energy densities.

Lithium metal which owns the high theoretical capacity (3,860 mAh·g^{-1}) and very low redox potential (−3.04 V vs. standard hydrogen electrode, SHE), is considered an ideal candidate to maximize the energy density of ASSBs [14, 17, 127]. According to the theoretical work by Newman that dendrite proliferation can be settled once the modulus of separators reaches 7 GPa, it was also proposed that the sulfide SEs with rigidity could suppress the dendrite hazards [128, 129]. However, studies revealed that the safety concerns caused by severe dendrite growth still existed, restricting its commercialization. Kasemchainan et al. reported that the creep of lithium metal was slower than its electrochemical stripping when combining with sulfide SEs at low pressure, causing voids to form at the lithium–sulfide interface [130]. The mismatch between lithium ion flux and lithium metal deformation eventually leads to the production of dendrites. In addition, although the critical current density of lithium metal has been greatly improved due to some excellent interfacial engineering or SE bulk modifications (e.g., improving from 0.4 to 1.4 mA·cm^{-1} for Li_6PS_5Cl, very recently, by Wang' group) [131], it still cannot compete with those in liquid organic electrolyte-based batteries [68]. In fact, we propose that the low columbic efficiency (CE) of lithium metal anodes with sulfide SEs could impede the employment of lithium metal anodes for this moment. A low CE at the lithium metal anode side indicates significant consumption of lithium-ion and electrolyte, which will irreversibly result in poor cycling stability and the end of cell life [132]. When the CE is 98%, for example, the residual lithium after 20 cycles is only 0.98^{20} = 66.76%, indicating a ~ 34% loss of lithium. For commercialization, a CE of 99.96% is necessary for cycling stability up to 500 cycles. However, the CE of lithium metal anodes with sulfide SEs is extremely low, and even could not be easily measured due to the severe interfacial side reaction. Up to now, only few work has discussed the CE value, in which the Li plating/stripping CE of pristine Li_3PS_4 was only 88% and LiF-rich SEI engineering could improve it to 98% [133]. It should be noted that the unsatisfied CE of 98% was achieved in lenient test conditions of 0.1 $mA\cdot cm^{-1}$ and 0.1 $mAh\cdot cm^{-1}$, indicating that there could be a much inferior CE value measured in more practical conditions such as 1 $mA\cdot cm^{-1}$ and 1 $mAh\cdot cm^{-1}$. As a result, it requires excessive amounts of lithium metal overused in ASSBs, reducing the overall energy density [134, 135]. The superiority of lithium metal anode can also supply Li source, so that the cathode can use high-capacity Li-free materials, such as S. However, due to both the low ionic and electric conductivities of S/Li_2S, it is necessary to use a big amount of carbon and sulfide SEs to ensure the electric and ionic conductive path in the cathode [136]. In a typical S cathode in ASSBs, the S content is always below 40% with an active mass loading of less than 1 $mg\cdot cm^{-2}$ which largely decreases the overall energy density. On the other hand, the complete solid to solid conversion mechanism makes the electrochemical reaction kinetics of the S cathode very slow. Usually, the sulfide based Li-S ASSBs need an operating temperature of around 50–60 °C to boost the reaction [123, 137]. It reveals that lithium metal application in ASSBs still faces various challenges, like the dendrite hazard, unstable interface, low critical current density, low CE and strict operating conditions.

Silicon anode which was first revealed in 1976, has gained tremendous attention due to its ultrahigh gravimetric capacity of 4,200 $mAh\cdot g^{-1}$ upon full lithiation to $Li_{4.4}Si$ [18, 19, 21]. The eco-friendly Si anode with an appropriate electrochemical potential of ~ 0.3 V (vs. Li^+/Li) can lead to a high working voltage satisfying batteries' high energy density. As shown in Fig. 9, Cao et al. compared the applications of Si anode and Li metal anode from four perspectives: cost, energy densities, interface compatibility, and processability [125]. At cost, Li is scarce on Earth, with an annual mining production of approximately 0.082 million tons in 2020 (excluding U.S. production). In comparison, the yearly manufacturing capacity of Si is 8.0 million tons, and the cost of Si metal is merely 2.1 thousand dollars per ton. The reducing cost of raw materials is beneficial for commercialization. The energy densities of ASSBs employing Li metal and Si anode are also assessed. With the current collectors and packing material fractions removed, the ASSBs using Si anode had gravimetric and volumetric energy densities of 356 $Wh\cdot kg^{-1}$ and 965 $Wh\cdot L^{-1}$, respectively, which are comparable to Li metal anode (410 $Wh\cdot kg^{-1}$ and 928 $Wh\cdot L^{-1}$) [125]. In terms of interface stability, Si is thermodynamically stable with sulfide SEs, and no passivation coatings are required to insulate Si and sulfide SEs. Dendrite formation is less likely due to Si's high working potential. From the processability, in order to ensure intimate contact between electrodes and electrolytes, an external stacking pressure is usually provided when constructing ASSBs. Under pressures greater than 25 MPa, however, Li metal quickly propagates through the SE and forms a short circuit [138]. In comparison, Si has a high Young's modulus of 130 GPa and is dimensionally stable when exposed to pressure [139]. In order to optimize the reaction kinetics and boost the critical current density, Li metal-based ASSBs usually require additional heating. In comparison, even at high current

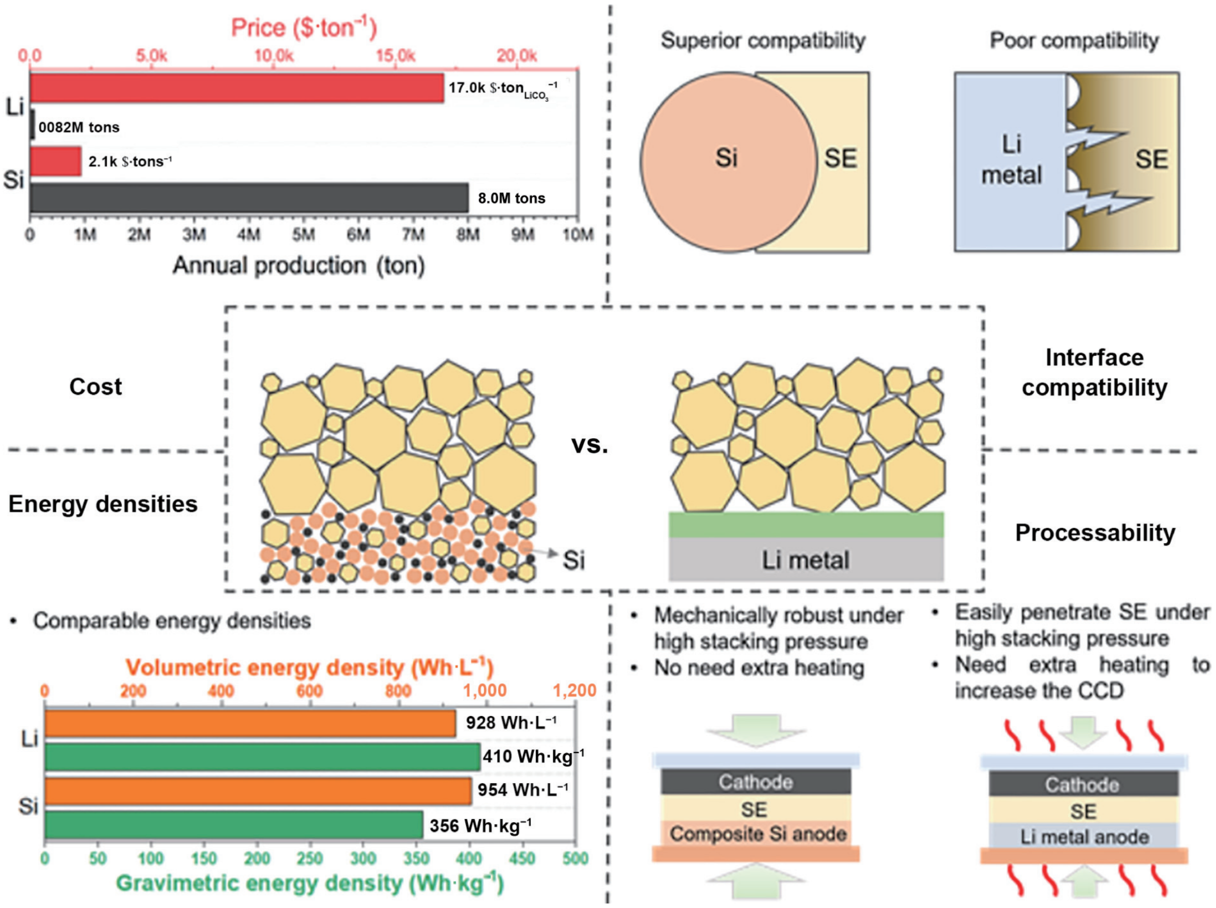

Figure 9 An evaluation of the Si anode and the Li metal anode in general. Cost, energy densities, interface compatibility, and processability of sulfide SE-based ASSBs are compared in the application of sulfide SE-based ASSBs. Reproduced with permission from Ref. [125], © Wiley-VCH GmbH 2022.

densities, the Si anode performs well at ambient temperature. Moreover, due to Si's superior air stability, anode fabrication could be done in a dry room rather than a glovebox. Li metal anode, in contrast, is restricted to a glovebox with a high-cost Argon atmosphere. The fabrication technique might be easily carried out using Si as an anode in a modified production line for present LIBs. Si anode-based ASSBs hold a lot of promise for large-scale energy storage applications, such as electric vehicles, as they provide high energy density, safety, reliability, and economic affordability.

3.2 The hindrance of silicon anode

Nowadays, research interest and commercial attempts of silicon anodes are mainly focused on their application in organic liquid electrolyte based LIBs, concerning about the notorious problems: (1) During lithiation, Si expands significantly in volume (e.g., 360% for $Li_{22}Si_5$ and 280% for $Li_{15}Si_4$), causing it to pulverize during cycling, separate from the current collector and lose electrical contact [140]. (2) Si's conductivity is not that high with an electrical conductivity of 1.56×10^{-3} $S{\cdot}m^{-1}$ and a lithium-ion diffusion coefficient of 10^{-14}–10^{-13} $cm^2{\cdot}s^{-1}$ [141]. (3) An unstable SEI layer forms in the liquid electrolyte. The electrode is protected from contact with the electrolyte by a thin SEI layer, resulting in further decomposition of the electrolyte. The SEI layer ruptures and exposes new active surfaces as the volume of silicon expands/contracts during cycling, continuously creating the SEI layer and consuming electrolytes as well as lithium-ions. The diffusion distance from lithium-ions rises as the SEI layer grows thicker, resulting a low cycle life and capacity retention [18, 20]. Despite of some excellent work including structural design of Si, preparation of Si-composite materials, design/selection of liquid electrolytes (e.g., solvent, salt and additives) and novel binders, the performance of pure Si active materials in liquid electrolytes is still not that satisfied [142, 143], so that the academia and industry chose to use limited Si mixed graphite anodes to weaken the influence of silicon volume expansion and SEI rupture, at the cost of energy density [19].

The problems of silicon anodes in liquid electrolyte based LIBs still exist in sulfide SE based ASSBs. However, from the respective characteristics of Si and sulfide, applying Si anodes with sulfide SEs could mitigate the problems of Si materials to some extent, which has a remarkable promoting effect on the realization of stable high-energy-density ASSBs [141]. First of all, sulfide SEs which have excellent mechanical ductility can contact intimately with the Si materials to provide sufficient ion conductions during the long-term cycling life of the ASSBs. The generating internal stress by Si's expansion could further improve the interfacial contact. Though the considerable volume change of Si during alloying/dealloying procedures is still unavoidable and can bring strain on the electrode, causing cracks to form, it was reported that the cracks were regularly vertical and could act as the volume buffer to some extent during Si's expansion/shrinkage procedures [125, 144]. Secondly, the applied external pressure design of sulfide based ASSBs can effectively maintain electron/ion transport inside electrodes, between Si particles and the Cu current collector, and at the electrode–SE interface, avoiding the "powder-off" issue. As a result, it allows the usage of minimum amount of binder in the Si anode in ASSBs to reduce ionic conductivity loss. Finally, the appropriate electrochemical potential of ~ 0.3 V vs. Li^+/Li, not only can lead to a high working voltage satisfying battery's high energy density, but also alleviate the interfacial side reaction with sulfides [145, 146].

The application of Si anode in sulfide based ASSBs was first developed by Lee's group in 2009 [147]. In earlier works, a large number of carbon conductive agents and sulfide materials were mixed in the Si anode to construct conductive pathways. The abuse of these inactive materials and the low Si mass loading (always below 1.5 $mg{\cdot}cm^{-1}$) impeded the advantage of high capacity of Si [144, 148–152]. The fabricated full cells always showed fast capacity decay with limited cycle life within dozens of cycles. Therefore, it showed relatively low study enthusiasm in the field and there are less than 90 research papers searching from "web of science" up to now.

Very recently, Meng's group reported the stable operation of a 99.9 wt.% micro-Si anode by using the interface passivating properties of sulfide SEs [23]. In their study, the sulfide materials did not permeate through the porous micro-Si anode, and the interfacial contact area between the SE and anode was reduced to a two-dimensional plane (Fig. 10). The reduced contact area significantly reduced the formation of SEI, decreasing the consumption of lithium-ion for a high CE. On the other hand, the detrimental role of conductive carbon for the serious side reaction with sulfide SEs was found and quantitatively evaluated by titration gas chromatography (TGC) technology. The abandon of carbon conductive agents in anode enabled improving cycling performance of micro-Si. It is proposed that the fundamental breakthrough could inspire a broad interest and bring a new research climax in sulfide SE-based ASSBs with silicon anode.

3.3 Key factors affecting compatibility of silicon with sulfide SE

Despite the fact that the ASSBs featuring Si anodes and sulfide SEs have a broad prospect, current research is still in its early stages, lacking a thorough understanding of fundamental scientific concerns. The problems like low electrical conductivity and lithium diffusion coefficient, drastic volume expansion upon alloying/dealloying and dynamic SEI layer generation still hinder the performance of silicon anodes in sulfide SE based ASSBs. In this section, we would review the major factors for Si based ASSBs revealed up to now, including the carbon effect, Si's particle size, pressure and sulfides' modules, the depth of Si's lithiation as well as the Si's composite matrix. We would also discuss the challenges and future direction of Si anode used in sulfide-based ASSBs, aiming to provide reference for accelerating the research progress in this field.

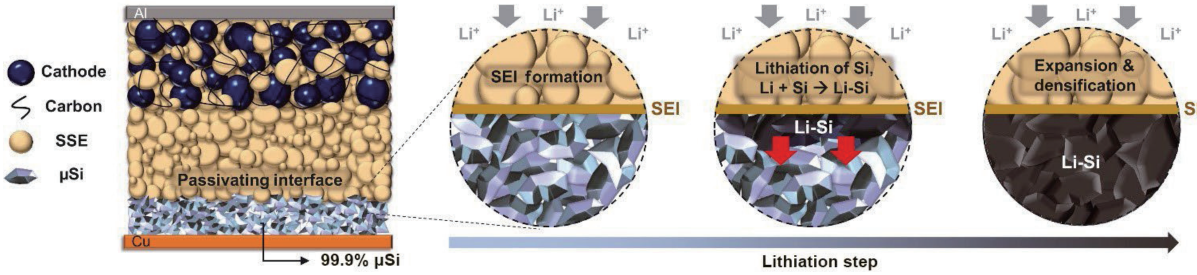

Figure 10 Schematic of 99.9 wt.% μSi electrode in an ASSB full cell. During lithiation, a passivating SEI is formed between the μSi and the sulfide SE, followed by lithiation of μSi particles near the interface. Reproduced with permission from Ref. [23], © Tan, D. H et al. 2021.

3.3.1 *The effect of carbon additive*

The carbon additive is universally used in electrodes of traditional LIBs to enhance the electronic conductivity for achieving high power densities and preventing overcharging [153]. When the ASSBs are operated in high current charging and discharging conditions, it is also important to add the carbon to construct the robust conductive path in electrodes [154]. In cathode side, it was reported even though the incorporation of carbon into the cathode composite favored a homogeneous current distribution, faster capacity decay was induced by the increase of the resistance derived from the accelerated decomposition of sulfide SEs. Janek's group revealed that the frequently-used carbon additives including ketjenback, graphite, acetylene black as well as C65, can indeed promote sulfide SEs to generate the S_8 and polysulfides, isolating the lithium-ion conduction routes. In the view of reaction kinetics, Tan et al. demonstrated that the replacement of high-surface-area carbon black with (80 $m^2 \cdot g^{-1}$) with lower-surface-area vapor-grown carbon fiber (24 $m^2 \cdot g^{-1}$) in cathode can suppress the side reaction [153]. Kim's group introduced that the oxygen-containing surface functional groups on the carbon species was an origin for causing negative effects on interfacial stability and the graphitic carbon showed better compatibility with sulfide SEs [155].

The carbon's decomposition effect at the anode was emphasized by Meng's study in 2021 [23]. Meng's group analyzed and quantified the SEI products from sulfide SE decomposition with and without the presence of carbon black. It showed that the cell without carbon black had an initial voltage plateau about 3.5 V, which is typical for a micro-Si||NCM811 cell. The cell with 20 wt.% carbon additive, however, exhibited a lower initial plateau at 2.5 V, indicating substantial sulfide electrochemical breakdown at the Si composite anode before reaching the lithiation potential above 3.5 V (Fig. 11(a)). Most of the pristine sulfide's signals in XRD were no longer present in the carbon-based cell, suggesting extensive electrolyte decomposition while Li_2S formed as a significant reductive product during cycling, as obvious peaks at 2θ angles of ~ 26°, 45°, and 52° appeared (Fig. 11(b)). In X-ray photoelectron spectroscopy (XPS) characterization, the peak with a binding energy consistent with Li-Si alloy was identified in the sample without carbon, whereas Si appeared to stay unreacted in the sample with carbon (Figs. 11(c)–11(e)). The phenomenon was attributed to the generation of lithium-ion consuming SEI products, which significantly restricted the lithiation of the micro-Si anode. The group thus fabricated the 99.9 wt.% micro-Si anode without any carbon additive to eliminate the side decomposition. The advanced TGC method was used to quantitatively evaluate the detrimental role of conductive carbon for the serious side reaction with sulfide SEs (Fig. 12(a)). First-cycle CE% of ~ 76% was measured across all cells, which quickly rose to > 99% from the second cycle (Fig. 12(b)). Fig. 12(c) depicts the amounts of SEI accumulated, active lithium-ion from Li-Si, cumulative losses, and overall cumulative capabilities. The total amount of SEI generated after the first cycle was determined to be 11.7% of the cell's capacity, increasing slightly to 12.4% in the second cycle. The

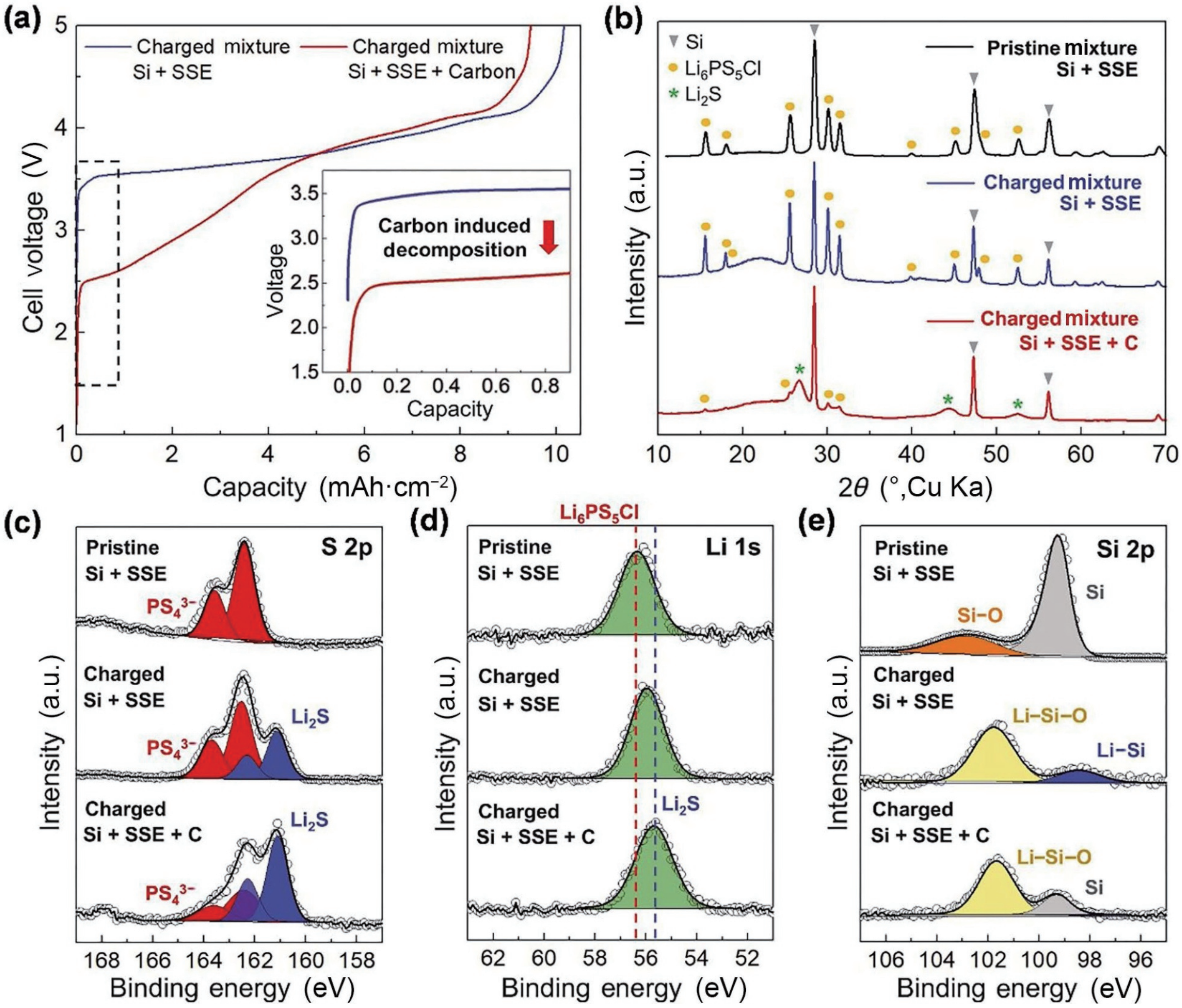

Figure 11 (a) Voltage profiles of μSi||Li_6PS_5Cl||NCM811 cells with and without carbon additives (20 wt.%). (b) XRD patterns. XPS spectra of the (c) S 2p, (d) Li 1s, and (e) Si 2p signals. Reproduced with permission from Ref. [23], © Tan, D. H. et al. 2021.

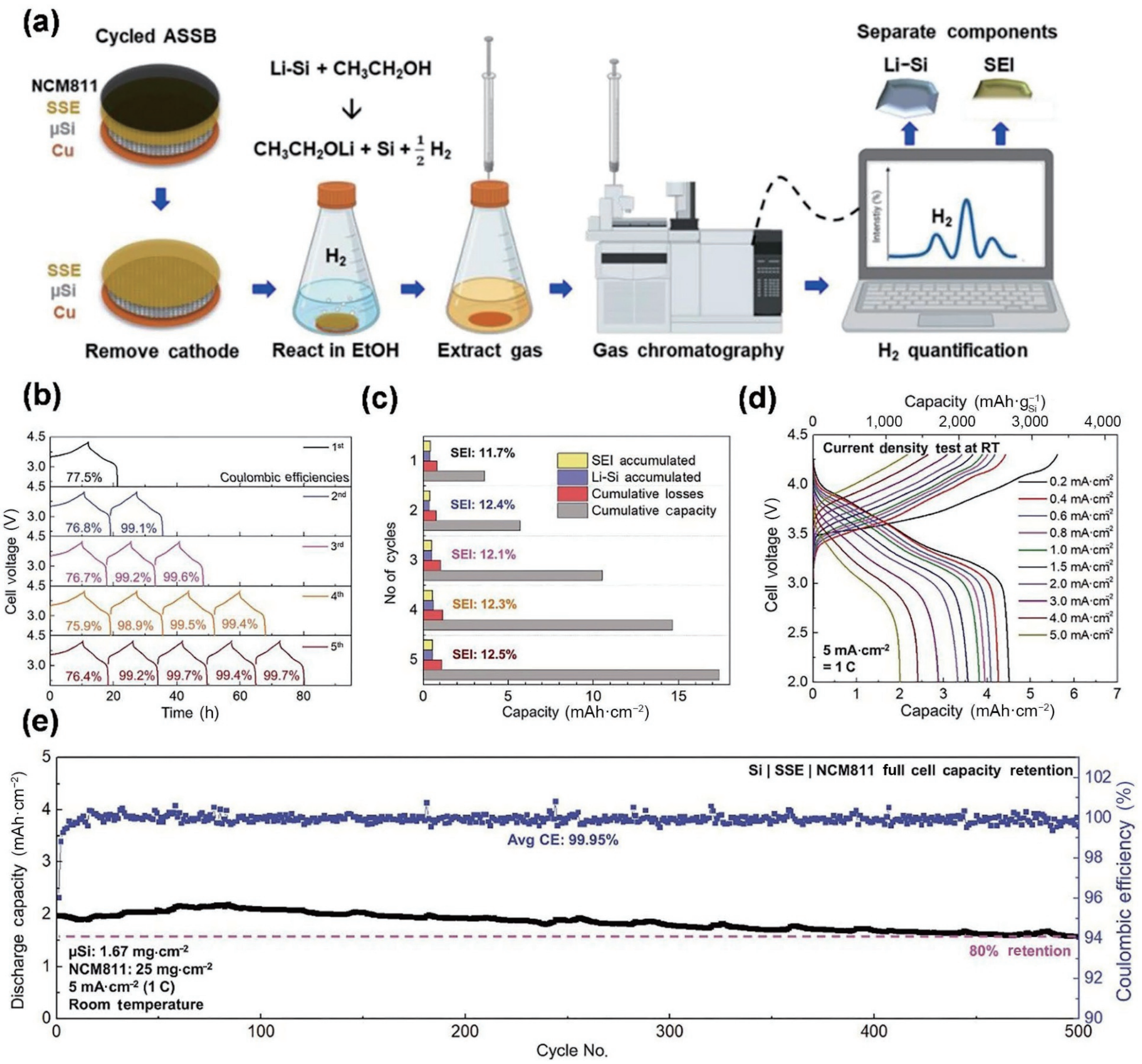

Figure 12 (a) Schematic of the procedure used to quantify the SEI growth at the lithiated μSi–SE interface by TGC technology. (b) and (c) Quantifying effects of SEI growth. (b) Voltage profiles of full cells used in titration gas chromatography. (c) Li-Si and SEI amounts relative to cell capacity. (d) The μSi||Li_6PS_5Cl||NCM811 performance of high current density test. (e) Cycle life at room temperature. Reproduced with permission from Ref. [23], © Tan, D. H. et al. 2021.

accumulated SEI and active lithium-ion remained stable and substantially unchanged in following cycles, showing interface passivation that inhibits undesirable ongoing interactions between Li-Si and the sulfide. As a result, the micro-Si||6PS5Cl||NCM811 full cell delivered a capacity retention of 80% after 500 cycles with an average CE of 99.95% (Fig. 12(d)).

As mentioned in Section 3.2, Si's conductivity is relatively low with an electrical conductivity of 1.56×10^{-3} S·m^{-1} and a lithium ion diffusion coefficient of 10^{-14}–10^{-13} cm^2·s^{-1}. The conductive additive is still necessary to ensure the composite anode's conductive pathways for better rate performance and higher Si mass loading. Takahashi's group reported that the Si anodes required a higher amount of conductive carbon than traditional graphite anode to form sufficient conduction pathways and a certain of acetylene black could improve the capacity retention especially under fast charging/discharging procedure [144]. Lee's group demonstrated that the Si anode with multiwalled carbon nanotubes (MWCNTs) delivered nearly a 100% increase after 100 cycles over comparable cells that instead employed acetylene black [150]. The improved conductive ability and the possibly intensified side reaction between Si and sulfide SEs with the increase of carbon additive should achieve balance.

Very recently, Kim's group demonstrated the diffusion-dependent Si electrode consisted of graphite (Fig. 13(a)) [154]. It seems that the graphite may be an ideal conductive carbon to satisfy both the high energy density and stability of ASSBs. The scanning electron microscopy (SEM) and energy dispersive X-ray spectroscopy (EDS) images of the electrode using graphite and silicon nanoparticles are shown in Figs. 13(d) and 13(e), demonstrating the uniform distribution of silicon particles owing to the dimensional feature. The electronic conductive graphite can support abundant electrons to neighboring Si which enables the stable electrochemical reactions. The graphite can not only well accommodate the volume change of Si owing to its structural robustness, but also play as one active material, contributing to the total capacity of the electrode. Furthermore, the graphite particles with much higher lithium diffusivity of 2.30×10^{-9} cm^2·s^{-1} can act as the media for lithium-ion transport to the silicon particles via the inter-diffusion (Figs. 13(b) and 13(c)). The calculated lithium-ion concentration demonstrated that the more available volume obtained by inter-diffusion at the increased interface in the nano-Si/graphite composite can be used for quick lithium ion transport, leading to reduced diffusion tortuosity of the electrode. Based upon the merits, the graphite included nano-Si anode delivered a high areal capacity of 2.76 mAh·cm^{-1} even at a high current density of 1.77 mA·cm^{-1} (Fig. 13(f)). However, there was no discussion into the compatibility of graphite and sulfide SEs. The decomposition mechanism between sulfide and Si anodes with

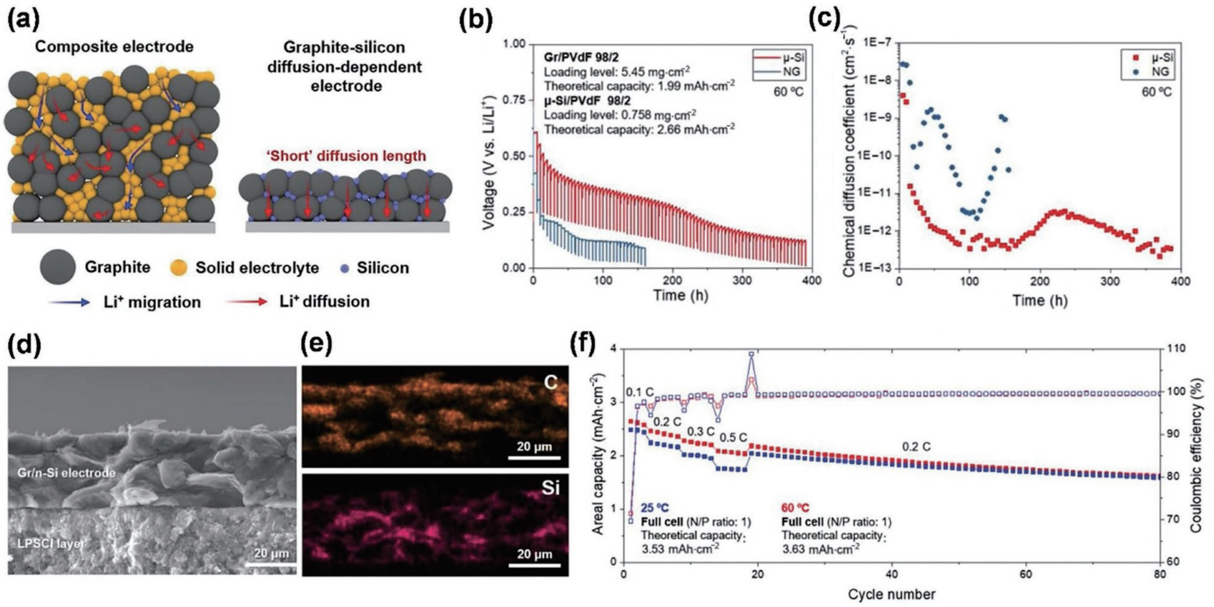

Figure 13 (a) Schematic diagram of the structure and lithium-ion transport of the composite electrode, and the graphite-silicon diffusion-dependent electrode. (b) Transient voltage profiles based on galvanostatic intermittent titration technique (GITT) for the diffusion-dependent electrodes. (c) The corresponding chemical diffusion coefficient of each electrode. (d) Cross-sectional SEM image of the graphite-silicon diffusion-dependent electrode. (e) The corresponding EDS results of the diffusion-dependent electrode. (f) Rate performance of the full cell employing the graphite-silicon diffusion-dependent electrode. Reproduced with permission from Ref. [154], © Wiley-VCH GmbH 2021.

various types of carbon should be understood and relative modification strategies required to be developed.

3.3.2 Si's particle size

The particle size of silicon materials is the key research interest in liquid-electrolyte based LIBs, and it still plays the vital role in ASSBs. From the experience in liquid electrolyte-based Si anodes, shrinking bulk Si to the nanoscale can minimize crack propagation by reducing the strain energy stored during electrochemical reactions, hence boosting structural stability and cycling lifetime [143]. In 2010, Trevey et al. first studied the effect of Si's particle size, and compared the electrochemical performance of nano-Si (50–100 nm) and bulk-Si (1–5 μm) in sulfide-based ASSBs [150]. It showed that the capacity of nano-Si was much higher than that of bulk-Si, with increased cycling stability. Dunlap et al. found the same trend in the coal-tar-pitch derived Si-C composite anode where the composite anode constructed with 50 nm Si particles outperformed the composites manufactured with micron-sized Si particles (1–3 μm and 325 mesh Si) in terms of first cycle capacity, CE value, and capacity retention (Fig. 14(a)) [149]. Obvious voids and separated interfaces can be observed in the cycled micro-Si containing electrode (Fig. 14(b)), which are detrimental to the electrochemical performance of the cell because they act as roadblocks to electrons and lithium-ion traveling through the electrode, increasing cell resistance. Compared to micro-Si electrodes, the 50 nm Si containing electrodes seemed much more compact with less cracks (Fig. 14(c)). Kim's group reported that the use of nanoscale Si resulted in uniform distribution throughout the composite electrode, increasing the contact surface capable of inter-diffusion between graphite and Si while reducing diffusion in agglomerated Si with low diffusivity [154]. The virtual 3D structures of graphite-Si composite electrodes showed that the nano-Si particles contact intimately with the graphite compared to the electrode fabricated with micro-Si particles (Figs. 14(d) and 14(e)). As summarized in Fig. 14(f), Si nanoparticles significantly enlarged the contact area with graphite particles from 1.73×10^{-9} to $5.26 \times 10^{-9} \cdot \mathrm{m}^2$, which is equivalent to near 200% increase. The morphology regulation reduced the lithium-ion diffusion in the agglomerated silicon, which considerably decreased the overpotential during cycling and boosted the specific capacities at higher current densities at 0.5 C rate (1.77 $\mathrm{mA \cdot cm^{-2}}$) with a large mass loading of 2.76 $\mathrm{mAh \cdot cm^{-2}}$. All these results demonstrate that the nano-Si active materials can outperform larger silicon particles in ASSBs using a dry electrode fabrication method due to their decreased diffusion distances and facile stress relaxation upon lithiation.

Modification and engineering of Si nanoparticle can further improve its performance. Okuno et al. first investigated the impact of nanopores in Si nanoparticles on the electrochemical performance [156]. Air-oxidation demagnesiation of Mg_2Si via mechanical milling of Mg_2Si and Mg and subsequent annealing were used to create nano-porous Si particles with an average pore size of 9.4 nm. Despite the huge size of Si of 506 nm in diameter, the nano-porous Si composite anodes retained about 80% of their capacity after 150 cycles while the capacity of nonporous Si composite anodes made up of Si particles with an average diameter of 466 nm faded dramatically after 10 cycles. As shown in Fig. 14(c), it demonstrated that the volumetric expansion of Si nanoparticles can be buffered by the shrinkage of the constructed nanopores and the elasticity of sulfide SEs relieved the strains arising from the expanded Si particles.

However, a set of important performance parameters in terms of gravimetric/volumetric capacity, CE value and electrode thickness, as well as areal capacity, should be completely evaluated to meet the requirements of practical cells for electrode materials. The construction of a dense electrode with a high density is critical for commercial viability. Porous Si particle is not an ideal choice, due to the low tap density. In particular, a dense electrode (e.g., $\rho = 1.0\ \mathrm{g \cdot cm^{-3}}$) requires only one-fifth the thickness of a loose electrode (e.g., $\rho = 0.2\ \mathrm{g \cdot cm^{-3}}$) to maintain the same areal mass loading [157]. A dense electrode, on the other hand, can accomplish several times the mass loading of a loose electrode with the same electrode thickness, considerably enhancing the areal capacity. In general, electrode density is directly related to particle size distribution, the porosity of material, active material volume percentage, and tap density, among which the tap density of active materials plays the essential role. In this regard, the application of high-tap-density microstructural Si (~ 1.3–1.6 $\mathrm{g \cdot m^{-3}}$) rather than

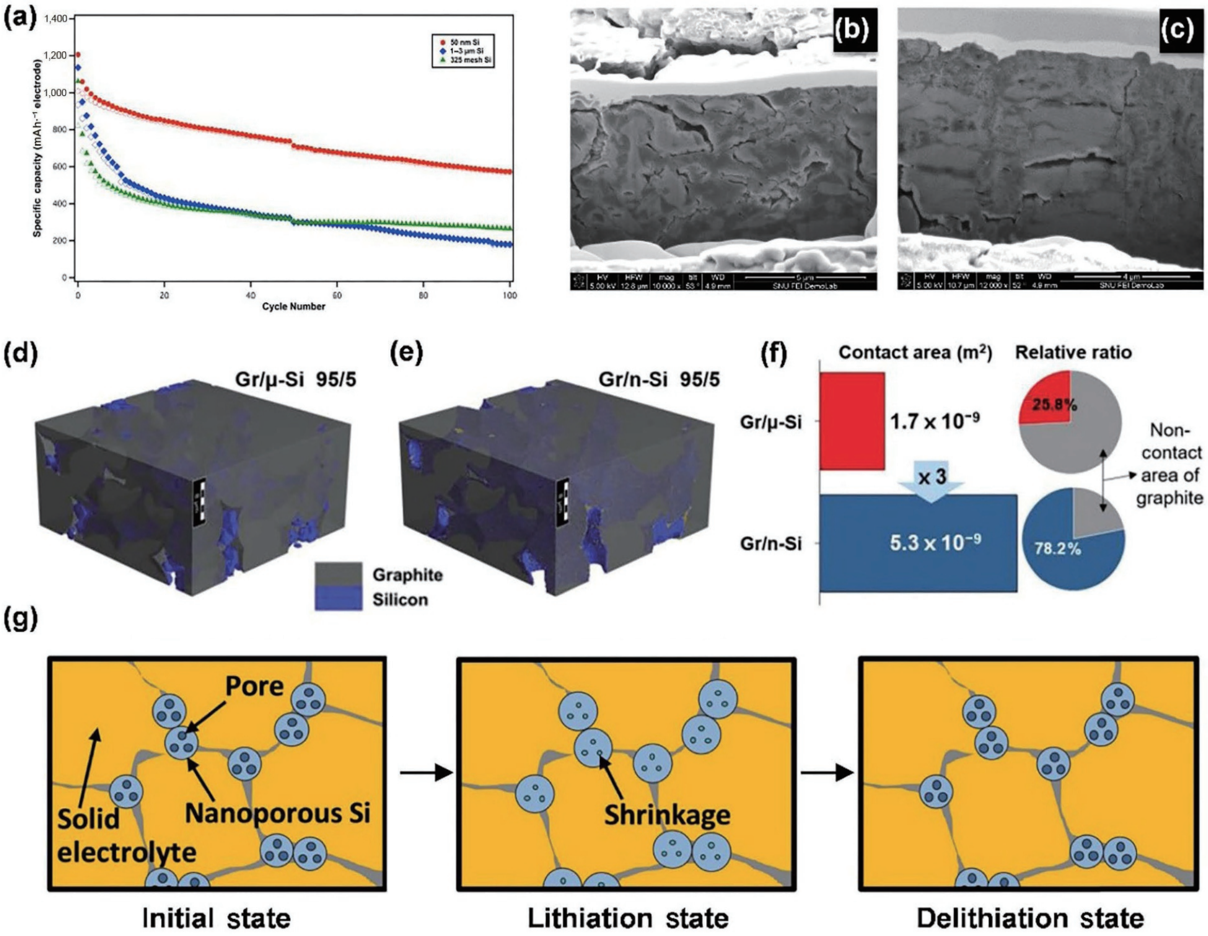

Figure 14 (a) Cycling performance of all-solid-state half-cells made containing 50 nm (red) 1–3 μm (blue) and 325 mesh (green) silicon particles. (b) and (c) Focused ion beam (FIB) cross-section view of composite electrodes after 100 cycles containing (b) 1–3 μm micro-Si electrode and (c) nano-Si electrode. (d) and (e) Digital twin-driven 3D structures of graphite-silicon electrodes of (d) μ-Si and (e) n-Si. (f) Contact area changes of silicon and graphite particles depending on silicon particle sizes in an absolute value (m²) and in the relative ratio (%). (g) Graphical illustrations of deformation processes of solid electrolytes in nanoporous Si-composite anodes. (a)–(c) Reproduced with permission from Ref. [149], © Elsevier B.V. 2018. (d)–(f) Reproduced with permission from Ref. [154], © Wiley-VCH GmbH 2021. (g) Reproduced with permission from Ref. [156], © Okuno, R. et al. 2020.

the low-tap-density nano-Si (0.1–0.2 g·m^{-3}) can hugely improve the volumetric energy density, gaining much attention of researchers [157–162]. Takahashi' group presented homogeneously dispersed composite sheets with micrometer-sized Si particles using a slurry-mixing approach [144]. The poly(propylene carbonate) (PPC) was used as a binder to disperse the slurry and keep the intimate contact of particles. Subsequent removal of the volatile binder by heating at 225 °C under vacuum from the composite was shown to reduce the electrode's internal resistance. In addition, the slurry coating method allowed to fabricate sheet-type ASSBs because it is scalable and benefits the control of the thickness of electrode and SE layers. As a result, the slurry fabricated micro-Si anode showed a high initial CE of 95% with desirable areal capacity of more than 2.0 mAh·cm^{-2}, and even exhibited the specific capacity above 1,700 mAh·g^{-1} after 375 cycles. Interestingly, it revealed that the slurry-mixing approach could enable the performance of micro-Si competing with that of nano-Si in sulfide based ASSBs. The similar conclusion was also presented by Jung's group using a sheet-type Li_6PS_5Cl-infiltrated nano-/micro-Si anodes fabricated by solution process [163]. The similar cycle performance of nano-/micro-Si in the slurry approach may be due to the generated passivation layer such as Li_2O, and lithium silicate formed during solution process that could prevent direct contact between the fresh surface of the expanded lithiated micro-Si and the sulfide SE. Unlike LIBs using the liquid electrolyte, it was also reported that the suitable external applied uniaxial pressure of dozens of MPa in ASSBs could help to prevent the easy purverization of micro-Si and electrode peel-off, increasing the performance of micro-Si [152].

3.3.3 *Pressure and sulfide' modules*

The external pressure has a great influence on the performance of silicon anodes in ASSBs. The mechanical confinement by the stress can enable the electrode particles to maintain good ion/electronic conductive path and prevent fractures of Si or electrode delamination during cycling. As the discussion in Section 2.4., a certain stress can also widen the electrochemical window of sulfide SEs towards more stable interfacial stability.

The electrochemical performance of Si anodes as a function of externally applied compressive stress was first introduced by Lee's group in 2012 [151]. They found that the specific capacity decreased with an increasing applied pressure. The cell at 3 MPa achieved a nearly theoretical capacity of 3,579 mAh·g^{-1} (for $Li_{15}Si_4$ at room temperature), whereas the capacity of 150 MPa cell decreased to ~ 2,800 mAh·g^{-1} and the 230 MPa cell only showed half as much as that in 3 MPa (Fig. 15(a)). However, the increased stress significantly improved the cycling stability of the cells. The capacity of the 3 MPa cell rapidly diminished with only 76.1% retention after 8 cycles while the 150 and 230 MPa cells still had 87.3% and 99% retention in the 21st cycle (Fig. 15(b)). Therefore, the lower capacity was countered by a more stable cycling behavior which was an attribute favored for battery materials. Large over-potential was found despite of the increase of bulk and interfacial conductivities under stress, resulting in the capacity

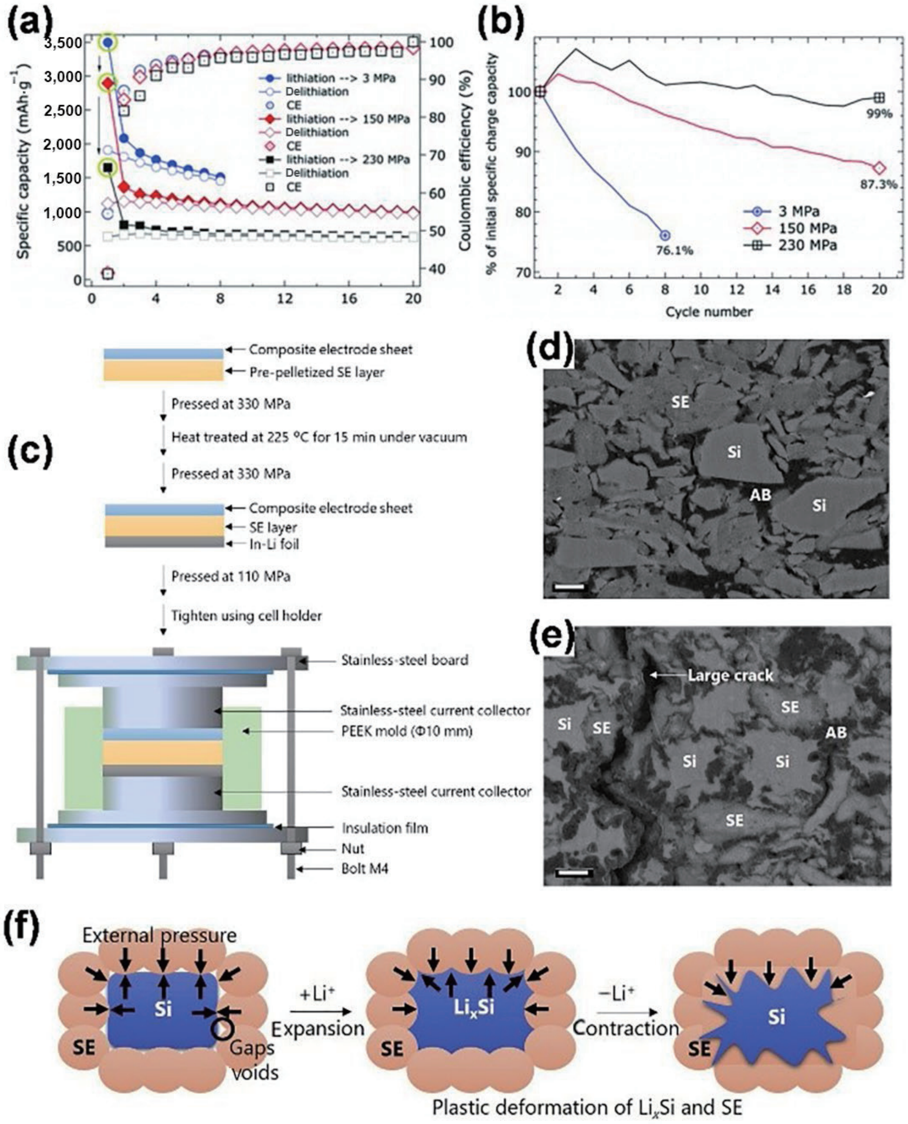

Figure 15 (a) Electrochemical performance and CE of solid-state nano-Si composite anodes cycled at a rate of C/20 under different compressive pressures. (b) Specific charge (delithiation) capacity retention as a percentage of initial specific capacity. (c) Schematic illustration of cell fabrication including a diagram of the tightening of a cell by a cell holder using bolts and nuts at three points. The applied pressure was adjusted by using a preset torque wrench, where the pressure was measured in advance by a load cell. (d) and (e) Cross-sectional SEM images of the Si-composite electrode under a compressive pressure of 75 MPa, which were disassembled after the (d) 3rd and (e) 150th charging cycles. Scale bars represent 1 μm. (f) Schematic diagram illustrating the process of the plastic deformation of Li_xSi and sulfide SE through repeated lithiation and delithiation. (a) and (b) Reproduced with permission from Ref. [151], © The Electrochemical Society 2012. (c)–(f) Reproduced with permission from Ref. [152], © Elsevier B.V. 2020.

limitation. The authors attributed the over-potential to the volume confinement of Si, where electric energy is expended to counteract the volumetric stains generated by Si's expansion, hindering the lithiation process. Unlike very low and very high compressive pressures that degrade battery performance, Takahashi' group reported that higher pressure could improve both the capacity and rate performance in the range of 15–75 MPa by maintaining ionic/electronic conductive pathways via particle interactions (Fig. 15(c)) [152]. From the microstructure analysis, they also revealed that pressure could facilitate plastic deformation of Li_xSi, resulting in the ameba-like shape for intimate contact to improve the charge-transfer kinetics (Figs. 15(d) and 15(e)). Si particles in an ASSB are surrounded by the sulfide SE matrix, which has gaps and voids, as shown in Fig. 15(f). As a result, Si particles are pressured in different ways. Li_xSi expands in the direction of the gaps and voids during lithiation. The Li_xSi is prone to contracting during future delithiation where it is being aggressively compressed by the SE. Plastic deformation of the Li_xSi and SE is caused by repeated expansions and contractions, especially under strong external pressures, resulting in the ameba-like structure observed. Tan et al. also found the enhanced cycling stability of full cells with the pressure increasing from 5 to 50 MPa [23]. Comprehensively, larger applied pressure can effectively optimize the electrical contact inside the electrode and benefit the delivery of Si's capacity when the compressive stress is less than the critical value. However, further increasing the pressure could restrict the volume expansion of Si, thus decreasing the capacity and may even intensify the pulverization Si particles. Hence, there exists an optimal external pressure which could vary with the types of sulfide materials. Any external pressure, from a commercial standpoint, necessitates more components in a cell and steps in the production plan, which would raise the cost. It was reported that low stack pressures, such as 2 MPa, could still be a burden in this case [53]. We here propose that the mechanical confinement provided by novel powerful binders or composite matrix could help to reduce the burden of applied external pressure.

The mechanical properties of sulfide SEs can also influence the performance of Si anodes. Tatsumisago's group studied the Li_2S-

P_2S_5 system with lithium halides [91]. When lithium halides were added to the glass electrolytes, the Young's moduli of the electrolytes decreased. In particular, the addition of LiI to the $0.75Li_2S$-$0.25P_2S_5$ glass gradually reduced its Young's modulus from 23 to 19 GPa. The lower bonding energy and ion packing density after LiI addition leaded to a reduction in the glass transition temperature of sulfide SEs, contributing to the drop of Young's moduli. The Si anode based cell with sulfide SEs including 30% LiI addition exhibited larger capacities over 20 cycles. As a result, it is expected that Li_2S-P_2S_5 glasses with improved mechanical properties, such as lower Young's modulus and higher formability could benefit the Si anode by building the intimate contact.

3.3.4 *Si's composite matrix*

The mechanical confinement can not only be achieved by external pressure, but also is available from the design of Si's anode matrix. Yersak et al. designed a silicon-titanium-nickel (STN) matrix to limit the extent of Si's lithiation, improving the reversibility of anodes [164]. The STN has a microstructure of nano-Si particle domains embedded in an electrochemically active $Ti_4Ni_4Si_7$ matrix. The matrix irreversibly takes up some lithium-ion during the initial lithiation of the STN alloy, resulting in a mixed conductor with a composition of roughly $Li_{3.2}Ti_4Ni_4Si_7$ and an ionic conductivity of 2.0 × 10^{-2} $mS{\cdot}cm^{-1}$. Due to the good ionic/electronic conductivity and the improved mechanical confinement of the STN matrix, the fabricated ASSB exhibited a stable specific capacity of 405 $mAh{\cdot}g^{-1}$ based on the overall mass of the composite electrode, which is over double the baseline, under a desirable external pressure of 3 MPa. In 2016, Lee's group reported the *in-situ* derived Sn-Si matrix anode where Sn can be lithiated prior to Si, and the pressure created by Sn's lithiation expansion was employed to confine Si materials, allowing for increased reversibility [165]. Moreover, because Sn is ductile and a good lithium ionic conductor, long-range interfaces between Sn and sulfide SEs were formed, minimizing interfacial resistance. Additionally, Sn does not decompose with the sulfide materials, allowing for greater stability. As a result, the capacity based the overall matrix anode achieved 700 $mAh{\cdot}g^{-1}$ with no obvious decay for 50 cycles. In spite of the stable performance, the Sn involved matrix increased the anode's potential to 0.53 V vs. Li^+/Li, which could decrease the energy density of ASSBs.

Meng's group proposed that the *in-situ* polymerization polyacrylonitrile (PAN) where the acrylonitrile (AN) monomer solution infiltrated Si's meso-pores to build the uniform Si@PAN matrix electrode [166]. It was reported that PAN was dehydrogenated and cyclized during the stabilization process to provide it delocalized sp^2 π bonding for intrinsic electronic conductivity, while avoiding full carbonization to keep the polymeric flexibility. Except for the role of mixed conductor, the PAN matrix behaved as a strong binder adhered to both the internal pores and the external bulk of micro-Si particles to suppress pulverization. Recently, Lee's group developed the electrochemically active soft carbon matrix by the pyrolysis of coal-tar-pitch which is a cheap industrial waste product [149]. The carbon matrix demonstrated excellent mixed conducting capacities and lithium-ion storage capacity as well as mechanically confinement ability. While it was determined that the amorphous carbon matrix was not robust enough to allow the long-term use of large micro-Si particles, the nano-Si composite electrode was optimized, resulting in a specific capacity of 653.5 $mAh{\cdot}g^{-1}$ based on composite electrode after 100th cycle with a CE of > 99%. Kim et al. developed Si nanoparticles embedded in a carbon nanofiber (CNF) matrix sheathed with LPSCl as the anode material for ASSBs with high energy density and stable cyclability [167]. More favorable strain release and robust electrical pathways were accessible by integrating Si in the carbon matrix. The interfacial stability between the active material and the SE was improved by the conformal coating of SEs on the surface of Si-C matrix, which leads to an improvement in electrochemical characteristics by reducing contact loss. After 50 cycles, the Si/CNF@LPSCl composite electrode delivered a reversible capacity of 1,172 $mAh{\cdot}g^{-1}$ and a stable cyclability of 84.3% at 0.5 C.

3.3.5 *The depth of Si's lithiation*

$Li_{15}Si_4$ is the highest lithiated phase available for the ambient temperature lithiation of bulk Si with a theoretical capacity of 3,579 $mAh{\cdot}g^{-1}$. The calculated density of this phase is 1.179 $g{\cdot}cm^{-3}$ based on X-ray measurements, indicating a huge volume expansion of 280% [140]. Krause' group proposed that by increasing the floor cut-off voltage to more than 50 mV, the generation of crystalline $Li_{15}Si_4$ could be prevented so that the huge volume change of the Si materials could be suppressed to realize the stable cycling of the electrode, though sacrificing part of the capacity [140]. In 2010, Lee's group verified this hypothesis in sulfide-based ASSBs. When the control cut-off voltage was larger than 50 mV vs. Li^+/Li, the batteries cycled obviously more steadily, although the reversible capacity dropped from 1,744 to 1,278 $mAh{\cdot}g^{-1}$ [150]. In 2020, the same group further evaluated the influence of Si's lithiation to PAN protected Si anode in ASSBs [148]. Notably, the cell with a 100 mV lower limit for Si delivered specific capacities of 1,606 $mAh{\cdot}g^{-1}$ after 200 cycles at 60 °C which corresponded to a 77.4% retention (Fig. 16(a)). While the initial capacity of the Si-PAN electrodes can be significantly increased by discharging to 5–50 mV in spite of rapid capacity loss during cycling.

The above research is based on Li||Si half ASSBs. Once the Si anode is fabricated with practical cathodes like NCM811 or $LiCoO_2$, the lithiation depth of Si anode cannot be directly observed or controlled. According to Jung's work, the three-electrode technology can be used to monitor the voltages of cathode and Si anode in time even for cells having thin sulfide SEs [168]. While precise control of the depth of lithiation of Si anode is considerably complicated in a full-cell configuration, Lee's group demonstrated that the lowering of the upper voltage during the charging of Si based full cells could reduce the depth of Si's lithiation, contributing the improved cycling stability (Fig. 16(b)) [148]. Another method is to appropriately increase the negative capacity:positive capacity ratio (n:p ratio) to reduce the Si's lithiation depth [169, 170]. It was demonstrated using a three-electrode ASSB cell arrangement that a larger n:p ratio of NCM||SE||Si-C cells led to stronger cathode delithiation as a result of the anode's higher cut-off voltage (lower utilization). As shown in Figs. 16(c) and 16(d), NCM||SE||Si-C full cells with a low (1.1 or 1.3) or high (2.0) n:p ratio had the best electrochemical performance, according to the examination of cell balancing. The pity is that both methods can theoretically reduce the energy density of the battery. However, due to the large specific capacity of silicon, the effect of such adjustment on the overall energy density could be limited. It is necessary to reach a compromise between the improved battery stability and the energy density by searching for the optimal upper charging voltage and n:p ratio.

4 Summary and perspective

ASSBs are now attracting fast-growing interests, especially due to their huge potential to overcome the safety issues of traditional LIBs and considerably improve the energy density. In summary, we systematically reviewed the most recent advances of ASSBs with sulfide SEs and Si anodes. The main challenges and

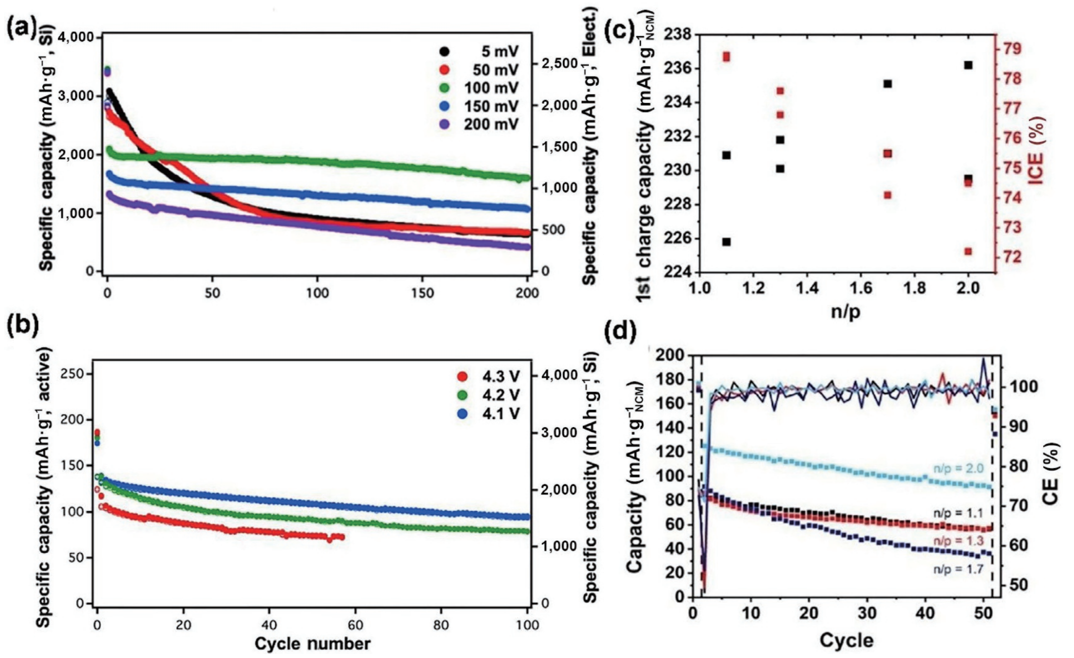

Figure 16 (a) Electrochemical performance of Si-PAN electrodes under different floor cut-off voltages. (b) Cycling performance of Si-PAN ||Li_6PS_5Cl||NCM811 full cells under different charging upper voltages. (c) First charge capacities and initial coulombic efficiencies (ICEs) of NCM||SE||Si-C full cells dependent on the n:p ratio. (d) Cycling performance of NCM||SE||Si-C full cells with different n:p ratios. (a) and (b) Reproduced with permission from Ref. [148], © The Electrochemical Society ("ECS") 2020. (c) and (d) Reproduced with permission from Ref. [169], © Poetke, S. et al. 2021.

corresponding strategies to realize high-performance ASSBs with sulfide SEs and Si anodes are proposed, aiming to offer a meaningful guideline to promote further research in this field.

Sulfide-based SEs are at the forefront of the energy technological transition, taking advantages of the remarkable ionic conductivity and deformability. The fundamental premise for the material design of sulfide SEs is a better understanding of their ionic conductivity and stable potential windows in respect to their elemental compositions and chemical bonding. The continuously optimized calculation method can provide the reference. Composition tuning, morphological control and interface modification are promising approaches to improve the electrochemical stability of sulfide SEs while maintaining the high ionic conductivity. The air stability of sulfide SEs is a particularly issue in large-scale manufacturing. Manipulating SE's bonding qualities based on HSAB theory has been a major focus to improving the air stability, and the methods like alkali metal oxide absorption, physical isolation via core–shell nanostructure design or polymer hybrids, specific crystal plane exposure and super hydrophobic coating have been also developed. However, exploiting practical air-stable sulfide SEs operated in a full life period in an ambient environment with economical and nontoxic raw materials is still urgent. The low elastic modulus of sulfide SEs allows for a cold-pressing process to reduce the grain boundary resistance for better battery performance. The elastic and shear moduli of sulfide SEs significantly benefit the interfacial compatibility with electrodes and fabrication process. "Zero-strain" electrode design, the addition of LiI to sulfide and filling the empty voids of sulfide particles with organic polymers can further release the stress during cycling or achieve higher mechanical flexibility. The improved mechanical stability of polymer-sulfide composite design is at the expense of the decreased ionic conductivity due to the covering of fast ion conductive sulfide's surface. Effectively improving the ionic conductivity of polymer/inorganic composite SEs to greater than 1 $mS \cdot cm^{-1}$ at room temperature is one of the key problems. The poor thermal stability of sulfide SEs requires lower synthesis or pressing temperature as higher temperature (> 300 ℃) significantly decreases the purity of the fast ionic conductor phase. Liquid-phase chemistry provides a new method to synthesize sulfide SEs at moderate temperature while the solvent stability of sulfides should be taken into consideration. Further efforts based on the fundamental study of the liquid-reaction mechanism are required to lower the temperatures to completely remove the organic solvent and avoid the ionic conductivity sacrifice.

The application of a Si anode in sulfide-based ASSBs combines the benefits of Si's huge capacity with sulfide SE's excellent ionic conductivity, resulting in a very promising energy storage device system that is still in its early stages. The carbon additive is necessary in the Si anode composites to enhance the electronic conductivity for achieving high power densities. However, the carbon's decomposition effect to the sulfide material was gradually revealed. It demonstrated that the graphite can be an appropriate conductive carbon to satisfy both the high energy density and stability of ASSBs. The decomposition mechanism between sulfides and Si anodes with various types of carbon should be understood and relative modification strategies required to be developed. The use of nanoscale Si resulted in uniform distribution throughout the composite electrode and facile stress relaxation upon lithiation, decreasing diffusion distances. The performance of the Si anode in ASSBs is heavily influenced by external pressure. From a business standpoint, any external pressure needs more components in a cell and steps in the production plan, raising the cost. Mechanical confinement offered by novel powerful binders or composite matrixes could aid in the reduction of external pressure. Novel cheap compression technology which could successfully apply uniform pressure in all directions, effectively reducing voids inside the composite sheets to a large extent like a warm isostatic press (WIP) method, should be further exploited [88]. The forbidden crystalline $Li_{15}Si_4$' generation can suppress the huge volume change of the Si materials to realize the stable cycling of the electrode, though sacrificing part of the capacity. Adjusting the n:p ratio and the upper voltage during the charging of Si based full cells under three-electrode monitor technology can help to control the depth of Si's lithiation. In addition, it is meaningful to discover whether the modification of

Si in liquid electrolyte based batteries (e.g., nano-structure design, surface coating, strong binder, and pre-lithiation technology) can be successfully transferred to ASSBs to further improve battery performance.

Despite the development of various techniques and advancements, the practical application of ASSBs with sulfide SEs and Si anodes still requires feasible strategies to realize the trade-off between large gravimetric/volumetric capacity, high CE value, and larger operation current density as well as stable long-term cycling. Also, the feasibility and cost of fabrication process in mass production should be taken into consideration. In the coming years, the community expects to witness the maturing of ASSB technology, boosting its practical competence to the point where it can complement the established LIB technology.

Acknowledgements

This work was supported by the National Key R&D Program of China (No. 2018YFA0209600), the National Natural Science Foundation of China (Nos. 22022813 and 21878268), and the Leading Innovative and Entrepreneur Team Introduction Program of Zhejiang (No. 2019R01006).

References

[1] Armand, M.; Tarascon, J. M. Building better batteries. *Nature* **2008**, *451*, 652–657.

[2] Wang, X.; Wang, X. Y.; Lu, Y. Y. Realizing high voltage lithium cobalt oxide in lithium-ion batteries. *Ind. Eng. Chem. Res.* **2019**, *58*, 10119–10139.

[3] Tian, Y. S.; Zeng, G. B.; Rutt, A.; Shi, T.; Kim, H.; Wang, J. Y.; Koettgen, J.; Sun, Y. Z.; Ouyang, B.; Chen, T. N. et al. Promises and challenges of next-generation “beyond Li-ion” batteries for electric vehicles and grid decarbonization. *Chem. Rev.* **2021**, *121*, 1623–1669.

[4] Zhang, S.; Li, S. Y.; Lu, Y. Y. Designing safer lithium-based batteries with nonflammable electrolytes: A review. *eScience* **2021**, *1*, 163–177.

[5] Zhang, P.; Lai, X. Q.; Shen, J. R.; Zhang, D. H.; Yan, Y. H.; Zhang, R.; Sheng, J.; Dai, K. W. Research and industrialization progress of solid-state lithium battery. *Energy Storage Sci. Technol.* **2021**, *10*, 896–904.

[6] Zhou, Z. H. ; Sun, T. ; Cui, J. ; Shen, X. ; Shi, C. ; Cao, S. ; Zhao, J. B. A homogenous solid polymer electrolyte prepared by facile spray drying method is used for room-temperature solid lithium metal batteries. *Nano Res.* in press, http://doi.org/10.1007/s12274-021-3683-6.

[7] Manthiram, A.; Yu, X. W.; Wang, S. F. Lithium battery chemistries enabled by solid-state electrolytes. *Nat. Rev. Mater.* **2017**, *2*, 16103.

[8] Liang, F.; Sun, Y. L.; Yuan, Y. F.; Huang, J.; Hou, M. J.; Lu, J. Designing inorganic electrolytes for solid-state Li-ion batteries: A perspective of LGPS and garnet. *Mater. Today* **2021**, *50*, 418–441.

[9] Wang, R.; Zhang, X. J.; Cai, Y. C.; Nian, Q. S.; Tao, Z. L.; Chen, J. Safety-reinforced rechargeable Li-CO_2 battery based on a composite solid state electrolyte. *Nano Res.* **2019**, *12*, 2543–2548.

[10] Webb, M. A.; Jung, Y.; Pesko, D. M.; Savoie, B. M.; Yamamoto, U.; Coates, G. W.; Balsara, N. P.; Wang, Z. G.; Miller, T. F. Systematic computational and experimental investigation of lithium-ion transport mechanisms in polyester-based polymer electrolytes. *ACS Cent. Sci.* **2015**, *1*, 198–205.

[11] Liang, J. W.; Li, X. N.; Wang, S.; Adair, K. R.; Li, W. H.; Zhao, Y.; Wang, C. H.; Hu, Y. F.; Zhang, L.; Zhao, S. Q. et al. Site-occupation-tuned superionic Li_xScCl_{3+x} halide solid electrolytes for all-solid-state batteries. *J. Am. Chem. Soc.* **2020**, *142*, 7012–7022.

[12] Wang, C. H.; Liang, J. W.; Jiang, M.; Li, X. N.; Mukherjee, S.; Adair, K.; Zheng, M.; Zhao, Y.; Zhao, F. P.; Zhang, S. M. et al. Interface-assisted *in-situ* growth of halide electrolytes eliminating interfacial challenges of all-inorganic solid-state batteries. *Nano Energy* **2020**, *76*, 105015.

[13] Zhang, X.; Zhang, L. C.; Zhang, W. X.; Ren, Z. H.; Huang, Z. G.; Hu, J. J.; Gao, M. X.; Pan, H. G.; Liu, Y. F. Nano-synergy enables highly reversible storage of 9.2 wt.% hydrogen at mild conditions with lithium borohydride. *Nano Energy* **2021**, *83*, 105839.

[14] Wu, J. H.; Liu, S. F.; Han, F. D.; Yao, X. Y.; Wang, C. S. Lithium/sulfide all-solid-state batteries using sulfide electrolytes. *Adv. Mater.* **2021**, *33*, e2000751.

[15] Kim, K. J.; Rupp, J. L. M. All ceramic cathode composite design and manufacturing towards low interfacial resistance for garnet-based solid-state lithium batteries. *Energy Environ. Sci.* **2020**, *13*, 4930–4945.

[16] Cao, D. X.; Zhao, Y. Y.; Sun, X.; Natan, A.; Wang, Y.; Xiang, P. Y.; Wang, W.; Zhu, H. L. Processing strategies to improve cell-level energy density of metal sulfide electrolyte-based all-solid-state Li metal batteries and beyond. *ACS Energy Lett.* **2020**, *5*, 3468–3489.

[17] Liu, D. H.; Bai, Z. Y.; Li, M.; Yu, A.; Luo, D.; Liu, W. W.; Yang, L.; Lu, J.; Amine, K.; Chen, Z. W. Developing high safety Li-metal anodes for future high-energy Li-metal batteries: Strategies and perspectives. *Chem. Soc. Rev.* **2020**, *49*, 5407–5445.

[18] Chae, S.; Xu, Y. B.; Yi, R.; Lim, H. S.; Velickovic, D.; Li, X. L.; Li, Q. Y.; Wang, C. M.; Zhang, J. G. A micrometer-sized silicon/carbon composite anode synthesized by impregnation of petroleum pitch in nanoporous silicon. *Adv. Mater.* **2021**, *33*, 2103095.

[19] Chae, S.; Choi, S. H.; Kim, N.; Sung, J.; Cho, J. Integration of graphite and silicon anodes for the commercialization of high-energy lithium-ion batteries. *Angew. Chem., Int. Ed.* **2020**, *59*, 110–135.

[20] Cao, C. T.; Abate, I. I.; Sivonxay, E.; Shyam, B.; Jia, C. J.; Moritz, B.; Devereaux, T. P.; Persson, K. A.; Steinrück, H. G.; Toney, M. F. Solid electrolyte interphase on native oxide-terminated silicon anodes for Li-ion batteries. *Joule* **2019**, *3*, 762–781.

[21] Eshetu, G. G.; Figgemeier, E. Confronting the challenges of next-generation silicon anode-based lithium-ion batteries: Role of designer electrolyte additives and polymeric binders. *ChemSusChem* **2019**, *12*, 2515–2539.

[22] Liu, L. L.; Xu, J. R.; Wang, S.; Wu, F.; Li, H.; Chen, L. Q. Practical evaluation of energy densities for sulfide solid-state batteries. *eTransportation* **2019**, *1*, 100010.

[23] Tan, D. H. S.; Chen, Y. T.; Yang, H. D.; Bao, W.; Sreenarayanan, B.; Doux, J. M.; Li, W. K.; Lu, B. Y.; Ham, S. Y.; Sayahpour, B. et al. Carbon-free high-loading silicon anodes enabled by sulfide solid electrolytes. *Science* **2021**, *373*, 1494–1499.

[24] Muramatsu, H.; Hayashi, A.; Ohtomo, T.; Hama, S.; Tatsumisago, M. Structural change of Li_2S-P_2S_5 sulfide solid electrolytes in the atmosphere. *Solid State Ionics* **2011**, *182*, 116–119.

[25] Kanno, R.; Murayama, M. Lithium ionic conductor thio-LISICON: The Li_2S-GeS_2-P_2S_5 system. *J. Electrochem. Soc.* **2001**, *148*, A742.

[26] Kamaya, N.; Homma, K.; Yamakawa, Y.; Hirayama, M.; Kanno, R.; Yonemura, M.; Kamiyama, T.; Kato, Y.; Hama, S.; Kawamoto, K. et al. A lithium superionic conductor. *Nat. Mater.* **2011**, *10*, 682–686.

[27] Oh, K.; Chang, D.; Lee, B.; Kim, D. H.; Yoon, G.; Park, I.; Kim, B.; Kang, K. Native defects in $Li_{10}GeP_2S_{12}$ and their effect on lithium diffusion. *Chem. Mater.* **2018**, *30*, 4995–5004.

[28] Rangasamy, E.; Liu, Z. C.; Gobet, M.; Pilar, K.; Sahu, G.; Zhou, W.; Wu, H.; Greenbaum, S.; Liang, C. D. An iodide-based $Li_7P_2S_8I$ superionic conductor. *J. Am. Chem. Soc.* **2015**, *137*, 1384–1387.

[29] Adeli, P.; Bazak, J. D.; Park, K. H.; Kochetkov, I.; Huq, A.; Goward, G. R.; Nazar, L. F. Boosting solid-state diffusivity and conductivity in lithium superionic argyrodites by halide substitution. *Angew. Chem., Int. Ed.* **2019**, *58*, 8681–8686.

[30] Dietrich, C.; Weber, D. A.; Sedlmaier, S. J.; Indris, S.; Culver, S. P.; Walter, D.; Janek, J.; Zeier, W. G. Lithium ion conductivity in Li_2S-P_2S_5 glasses-building units and local structure evolution during the crystallization of superionic conductors Li_3PS_4, $Li_7P_3S_{11}$ and $Li_4P_2S_7$. *J. Mater. Chem. A* **2017**, *5*, 18111–18119.

[31] Ujiie, S.; Hayashi, A.; Tatsumisago, M. Structure, ionic conductivity and electrochemical stability of Li_2S-P_2S_5-LiI glass and glass-ceramic electrolytes. *Solid State Ionics* **2012**, *211*, 42–45.

[32] Homma, K.; Yonemura, M.; Kobayashi, T.; Nagao, M.; Hirayama, M.; Kanno, R. Crystal structure and phase transitions of the lithium ionic conductor Li_3PS_4. *Solid State Ionics* **2011**, *182*, 53–58.

[33] Seino, Y.; Ota, T.; Takada, K.; Hayashi, A.; Tatsumisago, M. A sulphide lithium super ion conductor is superior to liquid ion conductors for use in rechargeable batteries. *Energy Environ. Sci.* **2014**, *7*, 627–631.

[34] Boulineau, S.; Courty, M.; Tarascon, J. M.; Viallet, V. Mechanochemical synthesis of Li-argyrodite Li_6PS_5X (X = Cl, Br, I) as sulfur-based solid electrolytes for all solid state batteries application. *Solid State Ionics* **2012**, *221*, 1–5.

[35] Bron, P.; Johansson, S.; Zick, K.; auf der Günne, J. S.; Dehnen, S.; Roling, B. $Li_{10}SnP_2S_{12}$: An affordable lithium superionic conductor. *J. Am. Chem. Soc.* **2013**, *135*, 15694–15697.

[36] Kato, Y.; Hori, S.; Saito, T.; Suzuki, K.; Hirayama, M.; Mitsui, A.; Yonemura, M.; Iba, H.; Kanno, R. High-power all-solid-state batteries using sulfide superionic conductors. *Nat. Energy* **2016**, *1*, 16030.

[37] Wang, C. H.; Liang, J. W.; Zhao, Y.; Zheng, M.; Li, X. N.; Sun, X. L. All-solid-state lithium batteries enabled by sulfide electrolytes: From fundamental research to practical engineering design. *Energy Environ. Sci.* **2021**, *14*, 2577–2619.

[38] Hayashi, A.; Hama, S.; Morimoto, H.; Tatsumisago, M.; Minami, T. Preparation of Li_2S-P_2S_5 amorphous solid electrolytes by mechanical milling. *J. Am. Ceram. Soc.* **2001**, *84*, 477–479.

[39] Mizuno, F.; Hayashi, A.; Tadanaga, K.; Tatsumisago, M. New, Highly ion-conductive crystals precipitated from Li_2S-P_2S_5 glasses. *Adv. Mater.* **2005**, *17*, 918–921.

[40] Deiseroth, H. J.; Kong, S. T.; Eckert, H.; Vannahme, J.; Reiner, C.; Zaiß, T.; Schlosser, M. Li_6PS_5X: A class of crystalline Li-rich solids with an unusually high Li^+ mobility. *Angew. Chem., Int. Ed.* **2008**, *47*, 755–758.

[41] Jung, W. D.; Kim, J. S.; Choi, S.; Kim, S.; Jeon, M.; Jung, H. G.; Chung, K. Y.; Lee, J. H.; Kim, B. K.; Lee, J. H. et al. Superionic halogen-rich Li-argyrodites using *in situ* nanocrystal nucleation and rapid crystal growth. *Nano Lett.* **2020**, *20*, 2303–2309.

[42] Choi, Y. S.; Lee, J. C. Electronic and mechanistic origins of the superionic conductivity of sulfide-based solid electrolytes. *J. Power Sources* **2019**, *415*, 189–196.

[43] Lin, Z.; Liu, Z. C.; Fu, W. J.; Dudney, N. J.; Liang, C. D. Lithium polysulfidophosphates: A family of lithium-conducting sulfur-rich compounds for lithium-sulfur batteries. *Angew. Chem., Int. Ed.* **2013**, *52*, 7460–7463.

[44] Wang, Y.; Richards, W. D.; Ong, S. P.; Miara, L. J.; Kim, J. C.; Mo, Y. F.; Ceder, G. Design principles for solid-state lithium superionic conductors. *Nat. Mater.* **2015**, *14*, 1026–1031.

[45] Zhang, Q.; Cao, D. X.; Ma, Y.; Natan, A.; Aurora, P.; Zhu, H. L. Sulfide-based solid-state electrolytes: Synthesis, stability, and potential for all-solid-state batteries. *Adv. Mater.* **2019**, *31*, 1901131.

[46] Yu, T.; Ke, B. Y.; Li, H. Y.; Guo, S. H.; Zhou, H. S. Recent advances in sulfide electrolytes toward high specific energy solid-state lithium batteries. *Mater. Chem. Front.* **2021**, *5*, 4892–4911.

[47] Wang, X. L.; Xiao, R. J.; Li, H.; Chen, L. Q. Oxygen-driven transition from two-dimensional to three-dimensional transport behaviour in β-Li_3PS_4 electrolyte. *Phys. Chem. Chem. Phys.* **2016**, *18*, 21269–21277.

[48] Ooura, Y.; Machida, N.; Naito, M.; Shigematsu, T. Electrochemical properties of the amorphous solid electrolytes in the system Li_2S-Al_2S_3-P_2S_5. *Solid State Ionics* **2012**, *225*, 350–353.

[49] Lee, Y.; Jeong, J.; Lee, H. J.; Kim, M.; Han, D.; Kim, H.; Yuk, J. M.; Nam, K. W.; Chung, K. Y.; Jung, H. G. et al. Lithium argyrodite sulfide electrolytes with high ionic conductivity and air stability for all-solid-state Li-ion batteries. *ACS Energy Lett.* **2021**, *7*, 171–179.

[50] Iwasaki, R.; Hori, S.; Kanno, R.; Yajima, T.; Hirai, D.; Kato, Y.; Hiroi, Z. Weak anisotropic lithium-ion conductivity in single crystals of $Li_{10}GeP_2S_{12}$. *Chem. Mater.* **2019**, *31*, 3694–3699.

[51] Hood, Z. D.; Wang, H.; Li, Y. C.; Pandian, A. S.; Parans Paranthaman, M.; Liang, C. D. The "filler effect": A study of solid oxide fillers with β-Li_3PS_4 for lithium conducting electrolytes. *Solid State Ionics* **2015**, *283*, 75–80.

[52] Zhao, F. P.; Liang, J. W.; Yu, C.; Sun, Q.; Li, X. N.; Adair, K.; Wang, C. H.; Zhao, Y.; Zhang, S. M.; Li, W. H. et al. A versatile Sn-substituted argyrodite sulfide electrolyte for all-solid-state Li metal batteries. *Adv. Energy Mater.* **2020**, *10*, 1903422.

[53] Lee, J.; Lee, T.; Char, K.; Kim, K. J.; Choi, J. W. Issues and advances in scaling up sulfide-based all-solid-state batteries. *Acc. Chem. Res.* **2021**, *54*, 3390–3402.

[54] Kimura, T.; Kato, A.; Hotehama, C.; Sakuda, A.; Hayashi, A.; Tatsumisago, M. Preparation and characterization of lithium ion conductive Li_3SbS_4 glass and glass-ceramic electrolytes. *Solid State Ionics* **2019**, *333*, 45–49.

[55] Liang, J. W.; Chen, N.; Li, X. N.; Li, X.; Adair, K. R.; Li, J. J.; Wang, C. H.; Yu, C.; Norouzi Banis, M.; Zhang, L. et al. $Li_{10}Ge(P_{1-x}Sb_x)_2S_{12}$ lithium-ion conductors with enhanced atmospheric stability. *Chem. Mater.* **2020**, *32*, 2664–2672.

[56] Hayashi, A.; Muramatsu, H.; Ohtomo, T.; Hama, S.; Tatsumisago, M. Improvement of chemical stability of Li_3PS_4 glass electrolytes by adding M_xO_y (M = Fe, Zn, and Bi) nanoparticles. *J. Mater. Chem. A* **2013**, *1*, 6320–6326.

[57] Liu, G. Z.; Xie, D. J.; Wang, X. L.; Yao, X. Y.; Chen, S. J.; Xiao, R. J.; Li, H.; Xu, X. X. High air-stability and superior lithium ion conduction of $Li_{3+3x}P_{1-x}Zn_xS_{4-x}O_x$ by aliovalent substitution of ZnO for all-solid-state lithium batteries. *Energy Storage Mater.* **2019**, *17*, 266–274.

[58] Zhu, Y. Z.; Mo, Y. F. Materials design principles for air-stable lithium/sodium solid electrolytes. *Angew. Chem., Int. Ed.* **2020**, *59*, 17472–17476.

[59] Kaib, T.; Haddadpour, S. M.; Kapitein, M.; Bron, P.; Schröder, C.; Eckert, H.; Roling, B.; Dehnen, S. New lithium chalcogenidotetrelates, LiChT: Synthesis and characterization of the Li^+-conducting tetralithium *ortho*-sulfidostannate Li_4SnS_4. *Chem. Mater.* **2012**, *24*, 2211–2219.

[60] Schnell, J.; Knörzer, H.; Imbsweiler, A. J.; Reinhart, G. Solid versus liquid-A bottom-up calculation model to analyze the manufacturing cost of future high-energy batteries. *Energy Technol.* **2020**, *8*, 1901237.

[61] Hayashi, A.; Muramatsu, H.; Ohtomo, T.; Hama, S.; Tatsumisago, M. Improved chemical stability and cyclability in Li_2S-P_2S_5-P_2O_5-ZnO composite electrolytes for all-solid-state rechargeable lithium batteries. *J. Alloys Compd.* **2014**, *591*, 247–250.

[62] Jung, W. D.; Jeon, M.; Shin, S. S.; Kim, J. S.; Jung, H. G.; Kim, B. K.; Lee, J. H.; Chung, Y. C.; Kim, H. Functionalized sulfide solid electrolyte with air-stable and chemical-resistant oxysulfide nanolayer for all-solid-state batteries. *ACS Omega* **2020**, *5*, 26015–26022.

[63] Li, J.; Chen, H. W.; Shen, Y. B.; Hu, C. J.; Cheng, Z. J.; Lu, W.; Qiu, Y. J.; Chen, L. W. Covalent interfacial coupling for hybrid solid-state Li ion conductor. *Energy Storage Mater.* **2019**, *23*, 277–283.

[64] Tan, D. H. S.; Banerjee, A.; Deng, Z.; Wu, E. A.; Nguyen, H.; Doux, J. M.; Wang, X. F.; Cheng, J. H.; Ong, S. P.; Meng, Y. S. et al. Enabling thin and flexible solid-state composite electrolytes by the scalable solution process. *ACS Appl. Energy Mater.* **2019**, *2*, 6542–6550.

[65] Kim, J. S.; Jeon, M.; Kim, S.; Lee, J. H.; Kim, B. K.; Kim, H. Structural and electronic descriptors for atmospheric instability of Li-thiophosphate using density functional theory. *Solid State Ionics* **2020**, *346*, 115225.

[66] Xu, J. R.; Li, Y. X.; Lu, P. S.; Yan, W. L.; Yang, M.; Li, H.; Chen, L. Q.; Wu, F. Water-stable sulfide solid electrolyte membranes directly applicable in all-solid-state batteries enabled by superhydrophobic Li^+-conducting protection layer. *Adv. Energy Mater.* **2021**, *12*, 2102348.

[67] Lu, P. S.; Liu, L. L.; Wang, S.; Xu, J. R.; Peng, J.; Yan, W. L.; Wang, Q. C.; Li, H.; Chen, L. Q.; Wu, F. Superior all-solid-state batteries enabled by a gas-phase-synthesized sulfide electrolyte with ultrahigh moisture stability and ionic conductivity. *Adv. Mater.* **2021**, *33*, 2100921.

[68] Wang, X. Y.; Li, S. Y.; Zhang, W. D.; Wang, D.; Shen, Z. Y.; Zheng, J. P.; Zhuang, H. L.; He, Y.; Lu, Y. Y. Dual-salt-additive electrolyte enables high-voltage lithium metal full batteries capable of fast-charging ability. *Nano Energy* **2021**, *89*, 106353.

[69] Wang, X. Y.; Chen, M.; Li, S. Y.; Zhao, C.; Zhang, W. D.; Shen, Z. Y.; He, Y.; Feng, G.; Lu, Y. Y. Inhibiting dendrite growth via regulating the electrified interface for fast-charging lithium metal anode. *ACS Cent. Sci.* **2021**, *7*, 2029–2038.

[70] Wang, L. G.; Dai, A.; Xu, W. Q.; Lee, S.; Cha, W.; Harder, R.; Liu, T. C.; Ren, Y.; Yin, G. P.; Zuo, P. J. et al. Structural distortion induced by manganese activation in a lithium-rich layered cathode. *J. Am. Chem. Soc.* **2020**, *142*, 14966–14973.

[71] Han, F. D.; Westover, A. S.; Yue, J.; Fan, X. L.; Wang, F.; Chi, M. F.; Leonard, D. N.; Dudney, N. J.; Wang, H.; Wang, C. S. High electronic conductivity as the origin of lithium dendrite formation within solid electrolytes. *Nat. Energy* **2019**, *4*, 187–196.

[72] Zhang, Z. H.; Chen, S. J.; Yang, J.; Wang, J. Y.; Yao, L. L.; Yao, X. Y.; Cui, P.; Xu, X. X. Interface re-engineering of $Li_{10}GeP_2S_{12}$ electrolyte and lithium anode for all-solid-state lithium batteries with ultralong cycle life. *ACS Appl. Mater. Interfaces* **2018**, *10*, 2556–2565.

[73] Ji, X.; Hou, S.; Wang, P. F.; He, X. Z.; Piao, N.; Chen, J.; Fan, X. L.; Wang, C. S. Solid-state electrolyte design for lithium dendrite suppression. *Adv. Mater.* **2020**, *32*, e2002741.

[74] Cheng, T.; Merinov, B. V.; Morozov, S.; Goddard, W. A. Quantum mechanics reactive dynamics study of solid Li-electrode/Li_6PS_5Cl-electrolyte interface. *ACS Energy Lett.* **2017**, *2*, 1454–1459.

[75] Jiang, W.; Yan, L. J.; Zeng, X. M.; Meng, X. J.; Huang, R. Z.; Zhu, X. X.; Ling, M.; Liang, C. D. Adhesive sulfide solid electrolyte interface for lithium metal batteries. *ACS Appl. Mater. Interfaces* **2020**, *12*, 54876–54883.

[76] Han, F. D.; Zhu, Y. Z.; He, X. F.; Mo, Y. F.; Wang, C. S. Electrochemical stability of $Li_{10}GeP_2S_{12}$ and $Li_7La_3Zr_2O_{12}$ solid electrolytes. *Adv. Energy Mater.* **2016**, *6*, 1501590.

[77] Zhu, Y. Z.; He, X. F.; Mo, Y. F. Origin of outstanding stability in the lithium solid electrolyte materials: Insights from thermodynamic analyses based on first-principles calculations. *ACS Appl. Mater. Interfaces* **2015**, *7*, 23685–23693.

[78] Schwietert, T. K.; Arszelewska, V. A.; Wang, C.; Yu, C.; Vasileiadis, A.; De Klerk, N. J. J.; Hageman, J.; Hupfer, T.; Kerkamm, I.; Xu, Y. L. et al. Clarifying the relationship between redox activity and electrochemical stability in solid electrolytes. *Nat. Mater.* **2020**, *19*, 428–435.

[79] Zhang, Z. X.; Zhang, L.; Yan, X. L.; Wang, H. Q.; Liu, Y. Y.; Yu, C.; Cao, X. T.; Van Eijck, L.; Wen, B. All-in-one improvement toward Li_6PS_5Br-based solid electrolytes triggered by compositional tune. *J. Power Sources* **2019**, *410–411*, 162–170.

[80] Hori, S.; Suzuki, K.; Hirayama, M.; Kato, Y.; Kanno, R. Lithium superionic conductor $Li_{9.42}Si_{1.02}P_{2.1}S_{9.96}O_{2.04}$ with $Li_{10}GeP_2S_{12}$-type structure in the Li_2S-P_2S_5-SiO_2 pseudoternary system: Synthesis, electrochemical properties, and structure-composition relationships. *Front. Energy Res.* **2016**, *4*, 38.

[81] Zhou, P. F.; Wang, J. B.; Cheng, F. Y.; Li, F. J.; Chen, J. A solid lithium superionic conductor $Li_{11}AlP_2S_{12}$ with a thio-LISICON analogous structure. *Chem. Commun.* **2016**, *52*, 6091–6094.

[82] Wu, F.; Fitzhugh, W.; Ye, L. H.; Ning, J. X.; Li, X. Advanced sulfide solid electrolyte by core−shell structural design. *Nat. Commun.* **2018**, *9*, 4037.

[83] Meng, X. B.; Meng, X. B. An overview of molecular layer deposition for organic and organic-inorganic hybrid materials: Mechanisms, growth characteristics, and promising applications. *J. Mater. Chem. A* **2017**, *5*, 18326–18378.

[84] Meng, X. B. Atomic layer deposition of solid-state electrolytes for next-generation lithium-ion batteries and beyond: Opportunities and challenges. *Energy Storage Mater.* **2020**, *30*, 296–328.

[85] Haruyama, J.; Sodeyama, K.; Han, L. Y.; Takada, K.; Tateyama, Y. Space-charge layer effect at interface between oxide cathode and sulfide electrolyte in all-solid-state lithium-ion battery. *Chem. Mater.* **2014**, *26*, 4248–4255.

[86] Liu, G. Z.; Lu, Y.; Wan, H. L.; Weng, W.; Cai, L. T.; Li, Z.; Que, X. C.; Liu, H. J.; Yao, X. Y. Passivation of the cathode-electrolyte interface for 5 V-class all-solid-state batteries. *ACS Appl. Mater. Interfaces* **2020**, *12*, 28083–28090.

[87] Oh, G.; Hirayama, M.; Kwon, O.; Suzuki, K.; Kanno, R. Bulk-type all solid-state batteries with 5 V Class $LiNi_{0.5}Mn_{1.5}O_4$ cathode and $Li_{10}GeP_2S_{12}$ solid electrolyte. *Chem. Mater.* **2016**, *28*, 2634–2640.

[88] Lee, Y. G.; Fujiki, S.; Jung, C.; Suzuki, N.; Yashiro, N.; Omoda, R.; Ko, D. S.; Shiratsuchi, T.; Sugimoto, T.; Ryu, S. et al. High-energy long-cycling all-solid-state lithium metal batteries enabled by silver-carbon composite anodes. *Nat. Energy* **2020**, *5*, 299–308.

[89] Zhang, W. B.; Schröder, D.; Arlt, T.; Manke, I.; Koerver, R.; Pinedo, R.; Weber, D. A.; Sann, J.; Zeier, W. G.; Janek, J. (Electro)chemical expansion during cycling: Monitoring the pressure changes in operating solid-state lithium batteries. *J. Mater. Chem. A* **2017**, *5*, 9929–9936.

[90] Li, Y.; Zhang, D. C.; Xu, X. J.; Wang, Z. S.; Liu, Z. B.; Shen, J. D.; Liu, J.; Zhu, M. Interface engineering for composite cathodes in sulfide-based all-solid-state lithium batteries. *J. Energy Chem.* **2021**, *60*, 32–60.

[91] Kato, A.; Yamamoto, M.; Sakuda, A.; Hayashi, A.; Tatsumisago, M. Mechanical properties of Li_2S-P_2S_5 glasses with lithium halides and application in all-solid-state batteries. *ACS Appl. Energy Mater.* **2018**, *1*, 1002–1007.

[92] Yu, S.; Schmidt, R. D.; Garcia-Mendez, R.; Herbert, E.; Dudney, N. J.; Wolfenstine, J. B.; Sakamoto, J.; Siegel, D. J. Elastic properties of the solid electrolyte $Li_7La_3Zr_2O_{12}$ (LLZO). *Chem. Mater.* **2016**, *28*, 197–206.

[93] Sakuda, A.; Hayashi, A.; Takigawa, Y.; Higashi, K.; Tatsumisago, M. Evaluation of elastic modulus of Li_2S-P_2S_5 glassy solid electrolyte by ultrasonic sound velocity measurement and compression test. *J. Ceram. Soc. Jpn.* **2013**, *121*, 946–949.

[94] Zhang, W. D.; Fan, L.; Tong, Z. M.; Miao, J. Z.; Shen, Z. Y.; Li, S. Y.; Chen, F.; Qiu, Y. C.; Lu, Y. Y. Stable Li-metal deposition via a 3D nanodiamond matrix with ultrahigh Young's modulus. *Small Methods* **2019**, *3*, 1900325.

[95] Koerver, R.; Zhang, W. B.; De Biasi, L.; Schweidler, S.; Kondrakov, A. O.; Kolling, S.; Brezesinski, T.; Hartmann, P.; Zeier, W. G.; Janek, J. Chemo-mechanical expansion of lithium electrode materials-on the route to mechanically optimized all-solid-state batteries. *Energy Environ. Sci.* **2018**, *11*, 2142–2158.

[96] Shin, B. R.; Nam, Y. J.; Oh, D. Y.; Kim, D. H.; Kim, J. W.; Jung, Y. S. Comparative study of TiS_2/Li-In all-solid-state lithium batteries using glass-ceramic Li_3PS_4 and $Li_{10}GeP_2S_{12}$ solid electrolytes. *Electrochim. Acta* **2014**, *146*, 395–402.

[97] Sakuda, A.; Hayashi, A.; Tatsumisago, M. Sulfide solid electrolyte with favorable mechanical property for all-solid-state lithium battery. *Sci. Rep.* **2013**, *3*, 2261.

[98] Cho, J.; Kim, G.; Lim, H.; Liu, M. L. Electrochemical properties of GeS_2-based glass-polymer composite electrolytes for lithium-Ion batteries. *J. Electrochem. Soc.* **1998**, *145*, 1949–1952.

[99] Whiteley, J. M.; Taynton, P.; Zhang, W.; Lee, S. H. Ultra-thin solid-state Li-ion electrolyte membrane facilitated by a self-healing polymer matrix. *Adv. Mater.* **2015**, *27*, 6922–6927.

[100] Nam, Y. J.; Cho, S. J.; Oh, D. Y.; Lim, J. M.; Kim, S. Y.; Song, J. H.; Lee, Y. G.; Lee, S. Y.; Jung, Y. S. Bendable and thin sulfide solid electrolyte film: A new electrolyte opportunity for free-standing and stackable high-energy all-solid-state lithium-ion batteries. *Nano Lett.* **2015**, *15*, 3317–3323.

[101] Wang, C. H.; Yu, R. Z.; Duan, H.; Lu, Q. W.; Li, Q. Z.; Adair, K. R.; Bao, D. N.; Liu, Y.; Yang, R.; Wang, J. T. et al. Solvent-free approach for interweaving freestanding and ultrathin inorganic solid electrolyte membranes. *ACS Energy Lett.* **2021**, *7*, 410–416.

[102] Weber, D. A.; Senyshyn, A.; Weldert, K. S.; Wenzel, S.; Zhang, W. B.; Kaiser, R.; Berendts, S.; Janek, J.; Zeier, W. G. Structural insights and 3D diffusion pathways within the lithium superionic conductor $Li_{10}GeP_2S_{12}$. *Chem. Mater.* **2016**, *28*, 5905–5915.

[103] Hood, Z. D.; Kates, C.; Kirkham, M.; Adhikari, S.; Liang, C. D.; Holzwarth, N. A. W. Structural and electrolyte properties of $Li_4P_2S_6$. *Solid State Ionics* **2016**, *284*, 61–70.

[104] Garcia-Mendez, R.; Mizuno, F.; Zhang, R. G.; Arthur, T. S.;

Sakamoto, J. Effect of processing conditions of 75Li_2S-25P_2S_5 solid electrolyte on its DC electrochemical behavior. *Electrochim. Acta* **2017**, *237*, 144–151.

[105] Kaup, K.; Zhou, L. D.; Huq, A.; Nazar, L. F. Impact of the Li substructure on the diffusion pathways in alpha and beta Li_3PS_4: An *in situ* high temperature neutron diffraction study. *J. Mater. Chem. A* **2020**, *8*, 12446–12456.

[106] Minami, K.; Mizuno, F.; Hayashi, A.; Tatsumisago, M. Structure and properties of the 70$Li_2S\cdot(30-x)P_2S_5\cdot xP_2O_5$ oxysulfide glasses and glass-ceramics. *J. Non-Cryst. Solids* **2008**, *354*, 370–373.

[107] Tatsumisago, M.; Hama, S.; Hayashi, A.; Morimoto, H.; Minami, T. New lithium ion conducting glass-ceramics prepared from mechanochemical Li_2S-P_2S_5 glasses. *Solid State Ionics* **2002**, *154–155*, 635–640.

[108] Hayashi, A.; Hama, S.; Minami, T.; Tatsumisago, M. Formation of superionic crystals from mechanically milled Li_2S-P_2S_5 glasses. *Electrochem. Commun.* **2003**, *5*, 111–114.

[109] Miura, A.; Rosero-Navarro, N. C.; Sakuda, A.; Tadanaga, K.; Phuc, N. H. H.; Matsuda, A.; Machida, N.; Hayashi, A.; Tatsumisago, M. Liquid-phase syntheses of sulfide electrolytes for all-solid-state lithium battery. *Nat. Rev. Chem.* **2019**, *3*, 189–198.

[110] Wang, H.; Hood, Z. D.; Xia, Y. N.; Liang, C. D. Fabrication of ultrathin solid electrolyte membranes of β-Li_3PS_4 nanoflakes by evaporation-induced self-assembly for all-solid-state batteries. *J. Mater. Chem. A* **2016**, *4*, 8091–8096.

[111] Calpa, M.; Rosero-Navarro, N. C.; Miura, A.; Tadanaga, K. Preparation of sulfide solid electrolytes in the Li_2S-P_2S_5 system by a liquid phase process. *Inorg. Chem. Front.* **2018**, *5*, 501–508.

[112] Hood, Z. D.; Wang, H.; Pandian, A. S.; Peng, R.; Gilroy, K. D.; Chi, M. F.; Liang, C. D.; Xia, Y. N. Fabrication of sub-micrometer-thick solid electrolyte membranes of β-Li_3PS_4 via tiled assembly of nanoscale, plate-like building blocks. *Adv. Energy Mater.* **2018**, *8*, 1800014.

[113] Phuc, N. H. H.; Totani, M.; Morikawa, K.; Muto, H.; Matsuda, A. Preparation of Li_3PS_4 solid electrolyte using ethyl acetate as synthetic medium. *Solid State Ionics* **2016**, *288*, 240–243.

[114] Phuc, N. H. H.; Yamamoto, T.; Muto, H.; Matsuda, A. Fast synthesis of Li_2S-P_2S_5-LiI solid electrolyte precursors. *Inorg. Chem. Front.* **2017**, *4*, 1660–1664.

[115] Phuc, N. H. H.; Morikawa, K.; Totani, M.; Muto, H.; Matsuda, A. Chemical synthesis of Li_3PS_4 precursor suspension by liquid-phase shaking. *Solid State Ionics* **2016**, *285*, 2–5.

[116] Ito, S.; Nakakita, M.; Aihara, Y.; Uehara, T.; Machida, N. A synthesis of crystalline $Li_7P_3S_{11}$ solid electrolyte from 1, 2-dimethoxyethane solvent. *J. Power Sources* **2014**, *271*, 342–345.

[117] Park, K. H.; Bai, Q.; Kim, D. H.; Oh, D. Y.; Zhu, Y. Z.; Mo, Y. F.; Jung, Y. S. Design strategies, practical considerations, and new solution processes of sulfide solid electrolytes for all-solid-state batteries. *Adv. Energy Mater.* **2018**, *8*, 1800035.

[118] Liu, Z. C.; Fu, W. J.; Payzant, E. A.; Yu, X.; Wu, Z. L.; Dudney, N. J.; Kiggans, J.; Hong, K. L.; Rondinone, A. J.; Liang, C. D. Anomalous high ionic conductivity of nanoporous β-Li_3PS_4. *J. Am. Chem. Soc.* **2013**, *135*, 975–978.

[119] Wu, L. P.; Liu, G. Z.; Wan, H. L.; Weng, W.; Yao, X. Y. Superior lithium-stable $Li_7P_2S_8I$ solid electrolyte for all-solid-state lithium batteries. *J. Power Sources* **2021**, *491*, 229565.

[120] Lee, J. E.; Park, K. H.; Kim, J. C.; Wi, T. U.; Ha, A. R.; Song, Y. B.; Oh, D. Y.; Woo, J.; Kweon, S. H.; Yeom, S. J. et al. Universal solution synthesis of sulfide solid electrolytes using alkahest for all-solid-state batteries. *Adv. Mater.* **2022**, *34*, 2200083.

[121] Wang, X. Y.; Zhang, W. D.; Wang, D.; Zhuang, H. L.; Li, S. Y.; Fan, L.; Li, L. L.; Wang, X.; He, Y.; Lu, Y. Y. Ionic liquid-reinforced carbon nanofiber matrix enabled lean-electrolyte Li-S batteries via electrostatic attraction. *Energy Storage Mater.* **2020**, *26*, 378–384.

[122] Wu, C. S.; Lou, J. T.; Zhang, J.; Chen, Z. Y.; Kakar, A.; Emley, B.; Ai, Q.; Guo, H.; Liang, Y. L.; Lou, J. et al. Current status and future directions of all-solid-state batteries with lithium metal anodes, sulfide electrolytes, and layered transition metal oxide cathodes. *Nano Energy* **2021**, *87*, 106081.

[123] Zhu, X. X.; Jiang, W.; Zhao, S.; Huang, R. Z.; Ling, M.; Liang, C. D.; Wang, L. G. Exploring the concordant solid-state electrolytes for all-solid-state lithium-sulfur batteries. *Nano Energy* **2022**, *96*, 107093.

[124] Jiang, W.; Zhu, X. X.; Huang, R. Z.; Zhao, S.; Fan, X. M.; Ling, M.; Liang, C. D.; Wang, L. G. Revealing the design principles of Ni-rich cathodes for all-solid-state batteries. *Adv. Energy Mater.* **2022**, *12*, 2103473.

[125] Cao, D. X. ; Sun, X. ; Li, Y. J. ; Anderson, A. ; Lu, W. Q. ; Zhu, H. L. Long-cycling sulfide-based all-solid-state batteries enabled by electrochemo-mechanically stable electrodes. *Adv. Mater.*, in press, https://doi.org/10.1002/adma.202200401.

[126] Lu, J.; Chen, Z. W.; Pan, F.; Cui, Y.; Amine, K. High-performance anode materials for rechargeable lithium-ion batteries. *Electrochem. Energy Rev.* **2018**, *1*, 35–53.

[127] Cai, W. L.; Yao, Y. X.; Zhu, G. L.; Yan, C.; Jiang, L. L.; He, C. X.; Huang, J. Q.; Zhang, Q. A review on energy chemistry of fast-charging anodes. *Chem. Soc. Rev.* **2020**, *49*, 3806–3833.

[128] Ferrese, A.; Newman, J. Mechanical deformation of a lithium-metal anode due to a very stiff separator. *J. Electrochem. Soc.* **2014**, *161*, A1350–A1359.

[129] Monroe, C.; Newman, J. The impact of elastic deformation on deposition kinetics at lithium/polymer interfaces. *J. Electrochem. Soc.* **2005**, *152*, A396.

[130] Kasemchainan, J.; Zekoll, S.; Spencer Jolly, D.; Ning, Z. Y.; Hartley, G. O.; Marrow, J.; Bruce, P. G. Critical stripping current leads to dendrite formation on plating in lithium anode solid electrolyte cells. *Nat. Mater.* **2019**, *18*, 1105–1111.

[131] Wan, H. L.; Zhang, J. X.; Xia, J. L.; Ji, X.; He, X. Z.; Liu, S. F.; Wang, C. S. F and N rich solid electrolyte for stable all-solid-state battery. *Adv. Funct. Mater.* **2022**, *32*, 2110876.

[132] Lin, Z.; Liu, T. X.; Ai, X. P.; Liang, C. D. Aligning academia and industry for unified battery performance metrics. *Nat. Commun.* **2018**, *9*, 5262.

[133] Fan, X. L.; Ji, X.; Han, F. D.; Yue, J.; Chen, J.; Chen, L.; Deng, T.; Jiang, J. J.; Wang, C. S. Fluorinated solid electrolyte interphase enables highly reversible solid-state Li metal battery. *Sci. Adv.* **2018**, *4*, eaau9245.

[134] Tian, Y.; An, Y. L.; Wei, C. L.; Jiang, H. Y.; Xiong, S. L.; Feng, J. K.; Qian, Y. T. Recently advances and perspectives of anode-free rechargeable batteries. *Nano Energy* **2020**, *78*, 105344.

[135] Weber, R.; Genovese, M.; Louli, A. J.; Hames, S.; Martin, C.; Hill, I. G.; Dahn, J. R. Long cycle life and dendrite-free lithium morphology in anode-free lithium pouch cells enabled by a dual-salt liquid electrolyte. *Nat. Energy* **2019**, *4*, 683–689.

[136] Pan, H.; Cheng, Z.; He, P.; Zhou, H. S. A review of solid-state lithium-sulfur battery: Ion transport and polysulfide chemistry. *Energy Fuels* **2020**, *34*, 11942–11961.

[137] Yao, X. Y.; Huang, N.; Han, F. D.; Zhang, Q.; Wan, H. L.; Mwizerwa, J. P.; Wang, C. S.; Xu, X. X. High-performance all-solid-state lithium-sulfur batteries enabled by amorphous sulfur-coated reduced graphene oxide cathodes. *Adv. Energy Mater.* **2017**, *7*, 1602923.

[138] Doux, J. M.; Nguyen, H.; Tan, D. H. S.; Banerjee, A.; Wang, X. F.; Wu, E. A.; Jo, C.; Yang, H. D.; Meng, Y. S. Stack pressure considerations for room-temperature all-solid-state lithium metal batteries. *Adv. Energy Mater.* **2020**, *10*, 1903253.

[139] Hopcroft, M. A.; Nix, W. D.; Kenny, T. W. What is the Young's modulus of silicon. *J. Microelectromech. Syst.* **2010**, *19*, 229–238.

[140] Obrovac, M. N.; Krause, L. J. Reversible cycling of crystalline silicon powder. *J. Electrochem. Soc.* **2007**, *154*, A103.

[141] Yan, W. L.; Wu, F.; Li, H.; Chen, L. Q. Application of Si-based anodes in sulfide solid-state batteries. *Energy Storage Sci. Technol.* **2021**, *10*, 821–835.

[142] Lee, J.; Moon, J.; Han, S. A.; Kim, J.; Malgras, V.; Heo, Y. U.; Kim, H.; Lee, S. M.; Liu, H. K.; Dou, S. X. et al. Everlasting living and breathing gyroid 3D network in Si@SiO_x/C nanoarchitecture for lithium ion battery. *ACS Nano* **2019**, *13*, 9607–9619.

[143] Tao, W.; Wang, P.; You, Y.; Park, K.; Wang, C. Y.; Li, Y. K.; Cao, F. F.; Xin, S. Strategies for improving the storage performance of

silicon-based anodes in lithium-ion batteries. *Nano Res.* **2019**, *12*, 1739–1749.

[144] Yamamoto, M.; Terauchi, Y.; Sakuda, A.; Takahashi, M. Slurry mixing for fabricating silicon-composite electrodes in all-solid-state batteries with high areal capacity and cycling stability. *J. Power Sources* **2018**, *402*, 506–512.

[145] Yamamoto, M.; Terauchi, Y.; Sakuda, A.; Takahashi, M. Binder-free sheet-type all-solid-state batteries with enhanced rate capabilities and high energy densities. *Sci. Rep.* **2018**, *8*, 1212.

[146] Oh, D. Y.; Kim, D. H.; Jung, S. H.; Han, J. G.; Choi, N. S.; Jung, Y. S. Single-step wet-chemical fabrication of sheet-type electrodes from solid-electrolyte precursors for all-solid-state lithium-ion batteries. *J. Mater. Chem. A* **2017**, *5*, 20771–20779.

[147] Trevey, J.; Jang, J. S.; Jung, Y. S.; Stoldt, C. R.; Lee, S. H. Glass-ceramic Li_2S-P_2S_5 electrolytes prepared by a single step ball billing process and their application for all-solid-state lithium-ion batteries. *Electrochem. Commun.* **2009**, *11*, 1830–1833.

[148] Dunlap, N. A.; Kim, J.; Guthery, H.; Jiang, C. S.; Morrissey, I.; Stoldt, C. R.; Oh, K. H.; Al-Jassim, M.; Lee, S. H. Towards the commercialization of the all-solid-state Li-ion battery: Local bonding structure and the reversibility of sheet-style Si-PAN anodes. *J. Electrochem. Soc.* **2020**, *167*, 060522.

[149] Dunlap, N. A.; Kim, S.; Jeong, J. J.; Oh, K. H.; Lee, S. H. Simple and inexpensive coal-tar-pitch derived Si-C anode composite for all-solid-state Li-ion batteries. *Solid State Ionics* **2018**, *324*, 207–217.

[150] Trevey, J. E.; Rason, K. W.; Stoldt, C. R.; Lee, S. H. Improved performance of all-solid-state lithium-ion batteries using nanosilicon active material with multiwalled-carbon-nanotubes as a conductive additive. *Electrochem. Solid-State Lett.* **2010**, *13*, A154.

[151] Piper, D. M.; Yersak, T. A.; Lee, S. H. Effect of compressive stress on electrochemical performance of silicon anodes. *J. Electrochem. Soc.* **2013**, *160*, A77–A81.

[152] Yamamoto, M.; Terauchi, Y.; Sakuda, A.; Kato, A.; Takahashi, M. Effects of volume variations under different compressive pressures on the performance and microstructure of all-solid-state batteries. *J. Power Sources* **2020**, *473*, 228595.

[153] Tan, D. H. S.; Wu, E. A.; Nguyen, H.; Chen, Z.; Marple, M. A. T.; Doux, J. M.; Wang, X. F.; Yang, H. D.; Banerjee, A.; Meng, Y. S. Elucidating reversible electrochemical redox of Li_6PS_5Cl solid electrolyte. *ACS Energy Lett.* **2019**, *4*, 2418–2427.

[154] Kim, J. Y.; Jung, S.; Kang, S. H.; Park, J.; Lee, M. J.; Jin, D.; Shin, D. O.; Lee, Y. G.; Lee, Y. M. Graphite-silicon diffusion-dependent electrode with short effective diffusion length for high-performance all-solid-state batteries. *Adv. Energy Mater.* **2021**, *12*, 2103108.

[155] Park, S. W.; Oh, G.; Park, J. W.; Ha, Y. C.; Lee, S. M.; Yoon, S. Y.; Kim, B. G. Graphitic hollow nanocarbon as a promising conducting agent for solid-state lithium batteries. *Small* **2019**, *15*, 1900235.

[156] Okuno, R.; Yamamoto, M.; Kato, A.; Takahashi, M. Stable cyclability caused by hghly dispersed nanoporous Si composite anodes with sulfide-based solid electrolyte. *J. Electrochem. Soc.* **2020**, *167*, 140522.

[157] Zhu, G. J.; Chao, D. L.; Xu, W. L.; Wu, M. H.; Zhang, H. J. Microscale silicon-based anodes: Fundamental understanding and industrial prospects for practical high-energy lithium-ion batteries. *ACS Nano* **2021**, *15*, 15567–15593.

[158] Li, Y. Z.; Yan, K.; Lee, H. W.; Lu, Z. D.; Liu, N.; Cui, Y. Growth of conformal graphene cages on micrometre-sized silicon particles as stable battery anodes. *Nat. Energy* **2016**, *1*, 15029.

[159] An, W. L.; Gao, B.; Mei, S. X.; Xiang, B.; Fu, J. J.; Wang, L.; Zhang, Q. B.; Chu, P. K.; Huo, K. F. Scalable synthesis of ant-nest-like bulk porous silicon for high-performance lithium-ion battery anodes. *Nat. Commun.* **2019**, *10*, 1447.

[160] Li, G.; Huang, L. B.; Yan, M. Y.; Li, J. Y.; Jiang, K. C.; Yin, Y. X.; Xin, S.; Xu, Q.; Guo, Y. G. An integral interface with dynamically stable evolution on micron-sized SiO_x particle anode. *Nano Energy* **2020**, *74*, 104890.

[161] Zhang, Y.; Zhang, R.; Chen, S. C.; Gao, H. P.; Li, M. Q.; Song, X. L.; Xin, H. L.; Chen, Z. Diatomite-derived hierarchical porous crystalline-amorphous network for high-performance and sustainable Si anodes. *Adv. Funct. Mater.* **2020**, *30*, 2005956.

[162] Chae, S.; Ko, M.; Park, S.; Kim, N.; Ma, J.; Cho, J. Micron-sized Fe-Cu-Si ternary composite anodes for high energy Li-ion batteries. *Energy Environ. Sci.* **2016**, *9*, 1251–1257.

[163] Kim, D. H.; Lee, H. A.; Song, Y. B.; Park, J. W.; Lee, S. M.; Jung, Y. S. Sheet-type Li_6PS_5Cl-infiltrated Si anodes fabricated by solution process for all-solid-state lithium-ion batteries. *J. Power Sources* **2019**, *426*, 143–150.

[164] Yersak, T. A.; Son, S. B.; Cho, J. S.; Suh, S. S.; Kim, Y. U.; Moon, J. T.; Oh, K. H.; Lee, S. H. An all-solid-state Li-ion battery with a pre-lithiated Si-Ti-Ni alloy anode. *J. Electrochem. Soc.* **2013**, *160*, A1497–A1501.

[165] Whiteley, J. M.; Kim, J. W.; Piper, D. M.; Lee, S. H. High-capacity and highly reversible silicon-tin hybrid anode for solid-state lithium-ion batteries. *J. Electrochem. Soc.* **2015**, *163*, A251–A254.

[166] Yersak, T. A.; Shin, J.; Wang, Z.; Estrada, D.; Whiteley, J.; Lee, S. H.; Sailor, M. J.; Meng, Y. S. Preparation of mesoporous Si@PAN electrodes for Li-Ion batteries via the *in-situ* polymerization of PAN. *ECS Electrochem. Lett.* **2015**, *4*, A33–A36.

[167] Kim, J.; Kim, C.; Jang, I.; Park, J.; Kim, J.; Paik, U.; Song, T. Si nanoparticles embedded in carbon nanofiber sheathed with Li_6PS_5Cl as an anode material for all-solid-state batteries. *J. Power Sources* **2021**, *510*, 230425.

[168] Nam, Y. J.; Park, K. H.; Oh, D. Y.; An, W. H.; Jung, Y. S. Diagnosis of failure modes for all-solid-state Li-ion batteries enabled by three-electrode cells. *J. Mater. Chem. A* **2018**, *6*, 14867–14875.

[169] Poetke, S.; Hippauf, F.; Baasner, A.; Dörfler, S.; Althues, H.; Kaskel, S. Nanostructured Si-C composites as high-capacity anode material for all-solid-state lithium-ion batteries. *Batteries Supercaps* **2021**, *4*, 1323–1334.

[170] Chen, Z.; Zhang, L.; Wu, X. K.; Song, K. F.; Ren, B. Z.; Li, T.; Zhang, S. J. Effect of N/P ratios on the performance of $LiNi_{0.8}Co_{0.15}Al_{0.05}O_2||SiO_x$/graphite lithium-ion batteries. *J. Power Sources* **2019**, *439*, 227056.